Rotation Sensing Using Atom Interferometry in a Magnetic Trap

Edward Russell Moan
New York, New York

B.S., Bates College, 2014

A Dissertation presented to the Graduate Faculty
of the University of Virginia in Candidacy for the Degree of
Doctor of Philosophy

Department of Physics

University of Virginia
July, 2020

Contents

List of Figures

Acknowledgments

I have come a long way in the past six years as a graduate student at UVA, and I owe that to a few dozen people, so I'll keep my acknowledgements here to the folks who had a huge influence. In no particular order, here goes...

My graduate career would never have come to pass without my undergraduate advisor at Bates College, Nathan Lundblad. We met my first semester at Bates when I was an intro lab student, and then I got to know Nathan in seven classes he taught throughout my four years. I was lucky to have him as an instructor, and even luckier to have him as an advisor. I feel a special connection to Nathan because I was there the first day he made a condensate in his lab. I was hooked on BEC physics that day near the end of my junior year, and I applied to graduate schools with the sincere plan of continuing in cold-atom physics. Nathan has continued to be an influence for me throughout graduate school. I have been able to bring some of his wisdom to my lab in Virginia, especially with respect to optical fibers (shout out to the fiber MOT, which actually comes up in this thesis), and I still have flashbacks to my senior year at Bates about the MOT insulator transition using condensates in 3D optical lattices. All the tools I learned at Bates have come in handy, and that is owed almost entirely to Nathan. It has been a pleasure being able to catch up at NASA meetings and

DAMOP, and I am proud to be an alum of Nathan's lab.

There are many people to thank within the UVA physics department. In particular, Peter Cline, Faye Safley, and Dawn Shifflett were always available to answer questions and keep the physics department running. I owe a lot to Will Fariss and David Wimer in the machine shop, who were a bottomless source of engineering wisdom. I also owe a great deal to my first year comrades-in-arms at UVA: Sina, Dave, Rajveer, Ben, Aaron, Christiana, Sanjay, and Eric. Adjusting to graduate school can be tricky, and I think we were all better scientists after going through it together.

I have overlapped with a handful of other Casslab folks, and I am grateful to every one of them for their unique perspective and intuition. Of those, I would like to explicitly acknowledge my biggest experimental-physics influence, Oat Arpornthip. As my predecessor, he was ready and willing to teach me everything he knew about the physics, the experiment, and the day-to-day grind. But oddly enough, Oat found a way to be more influential to my graduate school career by introducing me to fire trucks. More on that in a bit...

Most of all from my lab cohort, I need to thank Adam Fallon. It makes a huge difference to work well with your lab partners; it's even better when your lab partner becomes your best friend. I suppose we probably supported our local whiskey distillery more than our fair share, but we also came up with some of the best ideas for lab over drinks and video games (sorry Cass), so I think it comes out in a wash. Adam could explain most of the work discussed in this thesis, mainly because he had a lot to do with it. Some of the most important steps towards a working atom interferometer are owed to his input. I don't know what lies ahead for either of us, but I sure hope we get to work together again.

Along the way, I found a second family thanks to my lab partner, Oat, at Seminole Trail Volunteer Fire Department (STVFD). Everyone needs an extracurricular during graduate school, but I never imagined mine would be volunteering as a firefighter and EMT. Oat insisted on my visiting the station and put me 100 feet up in the tower. I was immediately sold, and four years later I am graduating as a Lieutenant of Oat's old crew. This is a hugely important part of my life, and it will always remain so, if for no other reason than driving fire trucks is amazing.

I want to thank my girlfriend, Alice Thomson, for helping me through my graduate school journey. Once a six-year graduate career is finished, we produce a tidy thesis documenting our work. But of course that is not the full story, and Alice can recount the daily struggles. She lived through the ups and downs that come with experimental research, from the day I took over for Oat to the day I defended this thesis. I also need to thank Alice for cajoling me into adopting our dog, Puc. She is a strange but loving creature, and an infinite source of frustration and joy. Thank you for being open to an adventure after UVA, and—no kidding—thank you for reminding me to eat.

In my penultimate paragraph, I want to thank my family, without whom this would not have been possible. Dede, Terry, and Shane remained an unwavering support system. Six years of graduate school is a bit long, and they were happy to hear me rant about classes, classmates, or research whenever I needed. I appreciate everything they did to get me to this point, and I promise to make more trips home now that I don't have a PhD thesis to finish writing.

Lastly, I want to thank my advisor, Cass Sackett. I think there are a few great qualities that a physics professor needs: pedagogical chops, experimental savvy, and

patience. Cass has all of these in spades. It would have been a lot tougher to get through my first and second year classes without Cass willing and able to help me through difficult problems. Cass appreciates that students benefit not from struggling and failing at problem-solving, but from practicing. As a research advisor, he was omnipresent for questions about theory, or to lend a hand in the lab. Fortunately for me, my work with Cass will continue as a postdoc.

Abstract

This dissertation documents the implementation of a dual Sagnac interferometer using atoms confined to a magnetic trap at the University of Virginia. This matter-wave interferometer serves as a proof-of-principle system for rotation sensing applications. The trap provides cylindrical symmetry to a ^{87}Rb Bose-Einstein condensate. We use Bragg laser pulses to split the condensate, and we are able to use the oscillatory motion of the atoms afterwards to characterize the trap in an effort to make it suitable for interferometry. We split the condensate such that two conjugate interferometers are implemented simultaneously to provide common-mode noise rejection, which isolates the rotation signal. Finally, we were able to demonstrate gyroscope operation by rotating the optical table on which the experiment was performed.

1 Introduction

"Go back? No good at all!
Go sideways? Impossible!
Go forward? Only thing to do!
On we go!"

— J. R. R. Tolkien, *The Hobbit*

This year marks the 25th year since the first Bose-Einstein Condensates (BECs) were produced at NIST-JILA, MIT, and Rice University [1–3]. Atomic physicists have used these ultracold gasses to study numerous phenomena, including superfluidity, condensed matter analogues with optical lattices, atom interferometry, and various others [4–6]. The quantum properties of a macroscopic coherent state makes condensates attractive for the development of practical applications with ultracold atoms. We have developed a BEC machine to measure small, physical rotations, with an eye towards inertial navigation technologies.

1.1 Inertial navigation

Accuracy and precision are crucial to any navigation technique for moving vehicles. The global positioning system (GPS) was groundbreaking for military and industry applications, and has certainly changed the way we navigate the world in our day-to-day lives. But GPS requires line-of-sight signals from four or more satellites, so it becomes confused by mountains and bad weather [7]. It is also vulnerable to interference by bad actors, who can "jam" GPS signals or trick the system such that the user believes she is in a different location than she is in reality. GPS is also less useful for vehicles like submarines, which have poor signal below sea level. Submarines are able to revert to a form of navigation known as dead reckoning, where the navigator uses the speedometer, compass heading, and an estimate of the effects of water currents, to make time-indexed measurements and map the vessel's location from the initial known position. With each measurement, the accuracy of the user's location is reduced, as the error is integrated over time.

Inertial navigation systems are a refinement of dead reckoning. With an accurate measurement of the vehicle's acceleration as a function of time, $\mathbf{a}(t)$, the user can determine her position with respect to an initial location. These systems require three components: a linear accelerometer, a rotation sensor, and an accurate clock. With increased accuracy and precision of these tools, such inertial navigation systems begin to look like reasonable alternatives to GPS.

This work focuses on the rotational component of an inertial navigation system. So far, systems have used mechanical gyroscopes or optical gyroscopes. Mechanical gyroscopes allow the user to read off the device's angle with respect to a fixed frame,

as the system remains at a constant global orientation. The drawback of mechanical systems is that the moving parts create friction, which causes drift. Optical gyroscopes are used in many modern inertial systems. These use the interference of light to measure rotation. The mechanism by which interference occurs is known as the Sagnac effect. The drawback of optical gyroscopes is their sensitivity and drift. The work described here is an effort towards a matter-wave rotation sensor. Matter-wave interferometers are intrinsically more sensitive and have demonstrated superior gyroscope performance [8–10], but the benefits have not been large enough to offset the substantial increase in apparatus size and complexity that atomic systems require. Our efforts are part of a program to demonstrate both improved performance and lower requirements in terms of size, weight, and power.

1.2 The Sagnac effect

Atom interferometry (AI) exploits the wave properties of matter. In the same way optical interferometers operate, a phase shift develops between two waves traveling along different paths, and can be measured as an interference pattern. AI has been used to probe numerous things, including measurements of the gravitation constant, the fine-structure constant, and has been proposed as a mechanism for detecting gravitational waves [11–13]. In optical interferometers, the output phase is measured by observing the intensity of the interfering fields. In AI systems, the phase shift determines the atom number. We use Bose-condensed atoms confined to a weak magnetic trap.

One effective technique used for rotation sensing is Sagnac interferometry, in which

a wave is split, traverses two paths that enclose an area, and then is recombined. The resulting interference signal depends on the rotation rate of the system and the area enclosed by the paths [14]. Some of these interferometers use atoms in free fall. These systems have impressive rotation sensitivity, but have several limitations that make that impractical for navigation applications. First and foremost, these systems are too large. Some operate in drop towers as high as 10 meters tall [15, 16], which is obviously not ideal if it is to be placed on a moving vehicle. Second, since the atoms are in free fall, if the moving vehicle has a large enough linear acceleration the atoms will run into the wall of the vacuum chamber and the measurement is lost. It has long been hoped that these problems might be overcome using atoms confined in a guiding potential or trap, as opposed to atoms falling in free space [17–19]. The trapping potential itself can also be an advantage if it can help control the trajectory of the atoms. With a highly-symmetric, tunable trap, the atoms can be manipulated to move in circular loops that enclose a large area [20]. That motivated the design and construction of our magnetic waveguide, which traps atoms in a cylindrically symmetric trap. The atoms can be made to move back and forth across the trap over distances up to 0.5 mm.

First, we should develop how the Sagnac effect produces a phase shift in an interferometer [21]. Consider the cartoon in Fig. 1.1. If the system is at rest, the two waves travel the same path length, and recombine constructively at the output. If the system is rotating in a direction perpendicular to the enclosed area, then the clockwise and counterclockwise path lengths are different, and a resulting phase shift will be observed on the output, as first demonstrated by Sagnac in 1913 in the search for ether [14].

The time required for the wave to travel an infinitesimal distance $d\ell$ is $d\ell/v$, where

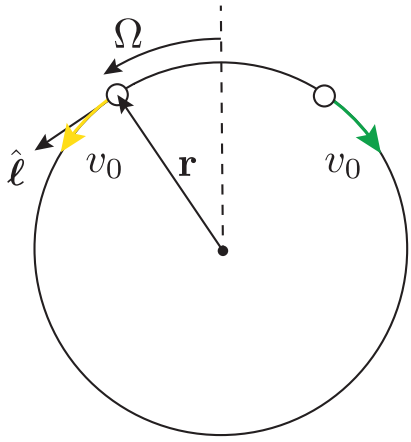

Figure 1.1: **A cartoon depiction of a Sagnac interferometer.** A wave is split at the top of the circle in opposite directions with equal speed. If the ring is rotating at $\Omega \neq 0$, the path length traversed by the yellow and green waves will be different. That causes a phase shift, which is proportional to the enclosed area of the ring and the angular speed, Ω.

v is the speed of the wave. With the system rotating at $\mathbf{\Omega}$, the component of the velocity due to rotation is

$$(\mathbf{\Omega} \times \mathbf{r}) \cdot \hat{\boldsymbol{\ell}}, \tag{1.1}$$

where $\mathbf{r}$ is the position and $\hat{\boldsymbol{\ell}}$ is a unit vector pointing along the path. If $\Omega \neq 0$, the change in the path length for the wave traveling clockwise is

$$\Delta\ell = \frac{1}{v} \oint_{\text{ring}} (\mathbf{\Omega} \times \mathbf{r})\, d\boldsymbol{\ell}. \tag{1.2}$$

We can apply Stoke's theorem to rewrite the integral in terms of an area differential, $d\mathbf{A}$,

$$\Delta\ell = \frac{1}{v} \int_{\text{ring}} \nabla \times (\mathbf{\Omega} \times \mathbf{r})\, d\mathbf{A}. \tag{1.3}$$

Equation (1.3) can be evaluated with an identity,

$$\nabla \times (\mathbf{\Omega} \times \mathbf{r}) = \mathbf{\Omega}(\nabla \cdot \mathbf{r}) - \mathbf{r}(\nabla \cdot \mathbf{\Omega}) + (\mathbf{r} \cdot \nabla)\mathbf{\Omega} - (\mathbf{\Omega} \cdot \nabla)\mathbf{r}. \tag{1.4}$$

The second and third terms are zero, since $\mathbf{\Omega}$ has no spatial dependence. Since $\nabla\cdot\mathbf{r} = 3$, the first term is $3\mathbf{\Omega}$. The last term is

$$(\mathbf{\Omega}\cdot\nabla)\mathbf{r} = (\Omega_x\partial_x + \Omega_y\partial_y + \Omega_z\partial_z)(x\,\hat{\mathbf{x}} + y\,\hat{\mathbf{y}} + z\,\hat{\mathbf{z}}) = \mathbf{\Omega} \tag{1.5}$$

Returning to Eq. (1.3) with these simplifications,

$$\Delta\ell = \frac{2}{v}\int_{\text{ring}} \mathbf{\Omega}\cdot d\mathbf{A} = \frac{2\,\mathbf{\Omega}\cdot\mathbf{A}}{v}. \tag{1.6}$$

The wave propagating counterclockwise has an oppositely-signed area vector, so the path length is $-\Delta\ell$. Therefore the overall phase is

$$\Delta\Phi = 2k\Delta\ell, \tag{1.7}$$

where k is the wavevector. In terms of the wavelength, λ,

$$\Delta\Phi = \frac{8\pi\,\mathbf{\Omega}\cdot\mathbf{A}}{\lambda v}. \tag{1.8}$$

In order to detect small rotations using laser light, the area enclosed has to be quite substantial, as the speed $v = c$. To measure the rotation rate of the Earth, for example, Michelson and Gale made an interferometer enclosing over 640 acres (1 square mile). Fiberoptic gyroscopes are made by coiling very long single-mode fibers around a cylinder to increase the enclosed area. First demonstrated in 1976 [22], these have developed enough to find practical applications in inertial navigation. In fiberoptic gyroscopes, the phase shift is internally converted to a frequency shift, which can be precisely measured. The advantage to matter-waves is that the velocity

is significantly lower. For the same rotation rate and enclosed area, the phase is 10^8 times larger than for an optical interferometer. This is certainly an advantage when measuring very small rotations.

A small number of trapped-atom Sagnac interferometers have been demonstrated in the past [23–27], but only recently have groups started making quantitative rotation measurements. The largest enclosed areas have been achieved using a linear interferometer that is translated along a direction perpendicular to the interferometer axis [24, 27], but this approach may not be well-suited for inertial measurements in a moving vehicle. The work in this thesis includes results from the first true two-dimension interferometer configuration in which atoms travel in circular trajectories through a static confining potential. This is one of a few experiments of its kind, but we report the largest enclosed Sagnac area of any such system to date [28], which we argue is easily scalable to larger areas and higher rotational sensitivities.

One key advance in this work is the use of dual counter-propagating interferometer measurements. Here, two Sagnac interferometers are implemented at the same time in the same trap, using atoms traveling with opposite velocities over the same paths. This technique was developed for free-space interferometers [9] and allows common-mode rejection of phase noise that can otherwise mask the rotation signal. The Sagnac effect itself is differential and can be extracted by comparing the two individual measurements. This technique is likely to be essential for a practical rotation-sensing system.

1.3 Scope

This thesis entails the summary of the experimental procedures for characterizing the magnetic potential in order to achieve a dual-Sagnac interferometer for rotation sensing, followed by details of our initial rotation measurement.

Chapter 2: Experimental setup: An overview of BEC production of ^{87}Rb, from laser cooling in a magneto-optical trap through evaporatively cooling to a condensate. Major changes that have been made to the system are described in more detail, such as a new imaging system and new laser setups, though much of the experimental procedure remains the same from previous accounts [29]. Bragg splitting, the mechanism we use to split the condensate and achieve interferometry, is described.

Chapter 3: The magnetic waveguide: This chapter describes the atom trap used in this experiment, starting with an analytical development of the system. By examining the magnetic fields, the confining potential is calculated and non-idealities are considered. An account of the waveguide design is given, along with trajectory measurements used to characterize the trap and compare it with the analytical case. The chapter concludes with a description of how the condensate can be split into four clouds that propagate around the trap in a circle, which is the foundation for the Sagnac interferometer.

Chapter 4: Interference measurements: The penultimate chapter describes the atom interferometry work done in this experiment. Starting with a simple development of atom interferometry, several experimental test results are included to study how certain parameters impact the interference signal. The chapter concludes with dual-Sagnac interferometry, in which two sets of waves interfere in concert, revealing

a differential phase. That phase can be used to measure small rotations, which we were able to do by rotating the experiment.

Chapter 5: Future work: In the last chapter, some suggested improvements to this system are included. Much of the work here serves as proof-of-principle for a new lab venture, which aims to make a smaller, semi-portable version of this system. Some of the preliminary efforts towards that goal are included.

2 Experimental setup

This chapter summarizes the experimental apparatus used for the results presented here. A brief overview of BEC production is provided through the dc TOP trap, with a more detailed discussion of the trap used for interferometry to follow in the next chapter. This chapter concludes with an overview of some improvements made to the imaging system, as well as an introduction to Bragg splitting.

2.1 Bose-Einstein Condensates

Before delving into a discussion of atom interferometry, it is worth reviewing our procedure for making a BEC. Most of the system remains unchanged from previous work [29, 30] so many of the details need not be recounted here. Significant changes will be discussed more at length.

2.1.1 Laser system

This BEC machine was developed by Robert Horne and Robert Leonard, with some minor changes implemented by Oat Arpornthip. The original laser system included

three separate lasers: a Toptica diode laser (DLPro) and tapered amplifier (TA) provided the main laser cooling system, a home-built distributed feedback (DFB) was used as a repump laser, and a home-built diode laser served as the Bragg laser [29,30]. The work in this thesis was carried out with this original laser system, but since then several changes have been made recently to improve stability and reliability. Since those changes are substantial, they will be documented here. Adapted from Horne [29], Fig. 2.1 summarizes the whole laser system as it presently stands. The home-built saturated absorption setup used previously was replaced with a fiber coupled Toptica CoSy saturated absorption module. This requires the laser lock to modulate laser current, instead of an external magnetic field as before. The laser lock signal and feedback is now controlled with a Toptica Digilock. A small amount of power from the DLPro, about 3 mW of a total 50 mW, is taken from the DLPro output to provide the locking signal. The beam is sent through a double-pass AOM, used to modulate the laser frequency during the experiment. This is in parallel with the TA and in series with the lock signal. Arranging the elements this way maximizes the power available for the TA. The output of the double-pass AOM is sent to the CoSy and lock via a single-mode optical fiber. The fiber is a 2×2 single mode fiber splitter; the second output will be used for the new Bragg laser's offset lock, briefly described later on.

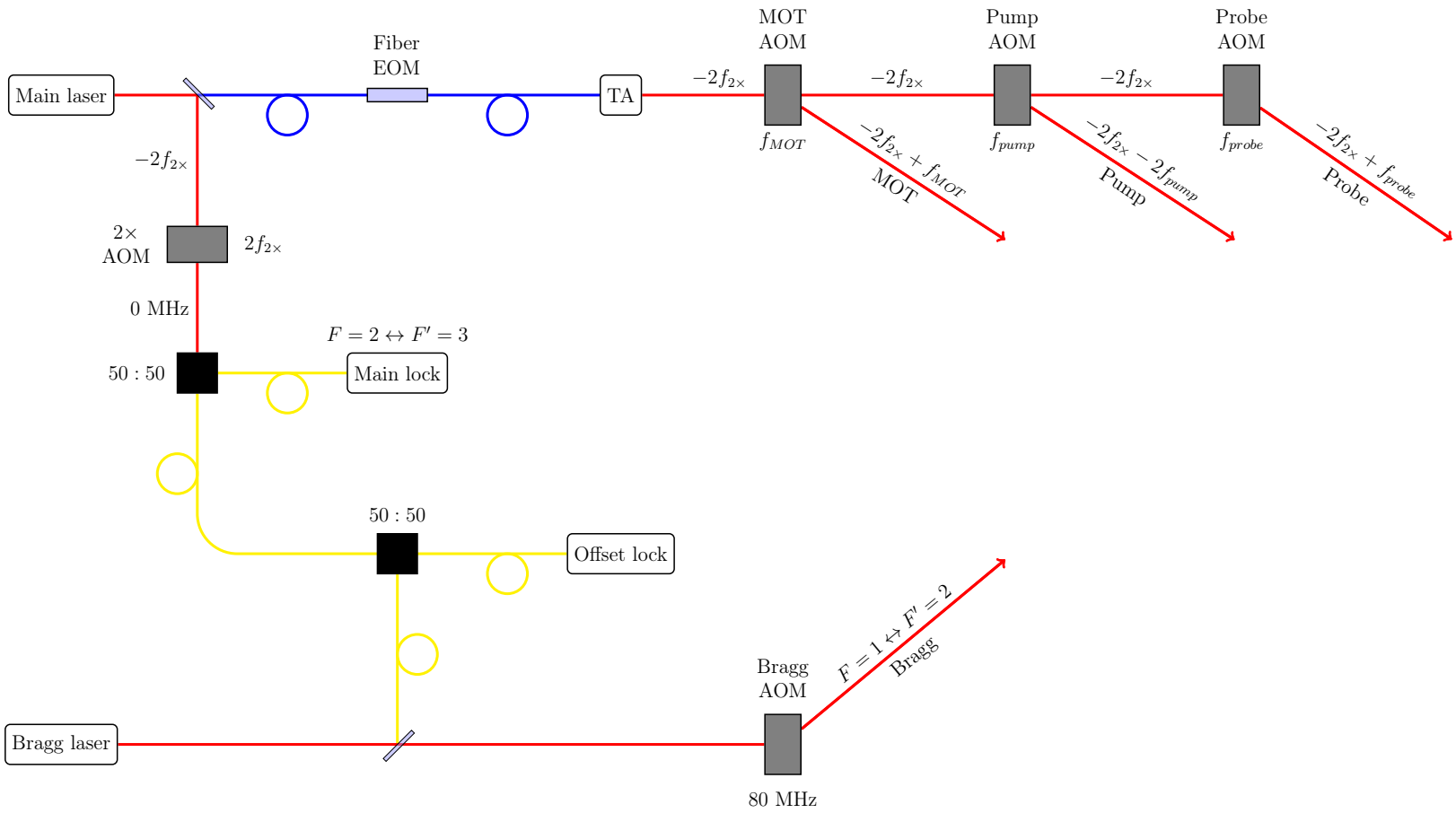

Figure 2.1: **A block diagram of the new laser system for future experiments.** Red lines are free-space lasers. Blue lines are polarization maintaining fibers, and yellow lines are single mode fibers. Changes to the previous setup include a fiber EOM which replaces the repump laser, and new locking setups for the DLPro and the new Bragg laser, which previously ran unlocked. Figure adapted from Horne [29].

AOM	AOM frequency (MHz)	$f_{2\times}$	Δf
MOT	+71.8	0 V	−20
Pumping	−160	1.0 V	−234.6
Probing	91.6	0	~ 0

Table 2.1: **AOM frequencies and laser detuning for different experimental stages.** The double pass AOM frequency, $f_{2\times}$, is set with an analog voltage to give continuous adjustment of the laser frequency. The offset frequency, Δf, is given with respect to the lock.

A repump laser is required to move atoms out of the dark state, $|5^2S_{1/2}\ F = 1\rangle$. Until recently, this was achieved with a separate repump laser locked using a second saturated absorption setup. To simplify the experiment, we now generate the repump light with a electro-optic modulator (EOM, AdvR WPM-K0780-P78P78AL3). The DLPro is now fiber coupled into the EOM, which adds side bands to the frequency spectrum, one of which is resonant with the reump transition 6.68 GHz blue-detuned from the cooling transition. The laser light leaving the EOM then seeds the TA, providing roughly 1.4 W of total power. A laser box encloses the whole system in order to eliminate unwanted stray light and to keep dust off the optics.

With different steps of the experiment requiring unique laser frequencies, the beam passes through several acousto-optic modulators (AOMs), each of which is associated with an experimental step. The AOMs also function as optical switches, in combination with mechanical shutters to block unwanted leakage light when the AOM is off. There are three AOMs associated with an experimental step: the MOT, optical pumping, and probing. Details of each step will follow this section chronologically; here we only characterize the laser states during each stage. The AOMs are included in the block diagram in Fig. 2.1, and the AOM setup and laser detuning from the cooling transition are detailed in Table 2.1.

It is also important that we can manipulate the EOM such that the repump tran-

State	Digital state	Frequency (GHz)	Relative power
MOT	↑↓	6.68	0.05
CMOT	↑↑	6.627	0.07
Pumping	↓↑	6.823	0.07
Probing	↓↓	off	0.00

Table 2.2: **A summary of the states of the EOM throughout the experiment.** The EOM is toggled between states with a multiplexer, controlled by two digital inputs. The relative power is measured against the power in the main carrier, and these are measured using the TA output's signal on a spectrum analyzer. The relative power are experimentally optimized for producing a BEC.

sition remains on resonance as the laser frequency is changed during the experiment. The EOM driver is documented in Fallon [31]. The driver allows the EOM to be switched between four unique states, each with a different frequency and power. The EOM can produce side bands with relative power from the main peak up to 15%. The four states are controlled by an internal multiplexer controlled by two digital inputs, and are summarized in Table 2.2.

The new Bragg laser is a Vescent D2-100-DBR, replacing our home-built system. The laser is locked using the D2-135 offset lock, using the DLPro as a reference frequency. About 0.5 mW of laser light from each laser is sent to an optical beat note detector, which provides feedback to the laser current. The offset lock is set up such that the Bragg laser is locked at the repump transition, around 7 GHz red-detuned from the main laser.

2.1.2 Magneto-optical trap

We start with ^{87}Rb atoms loaded into a magneto-optical trap (MOT). Atoms are loaded from a background thermal vapor provided by rubidium dispensers in a vacuum at 10^{-9} torr. We define the coordinate system such that $\hat{\mathbf{z}}$ points up, and $\hat{\mathbf{x}}$ and $\hat{\mathbf{y}}$

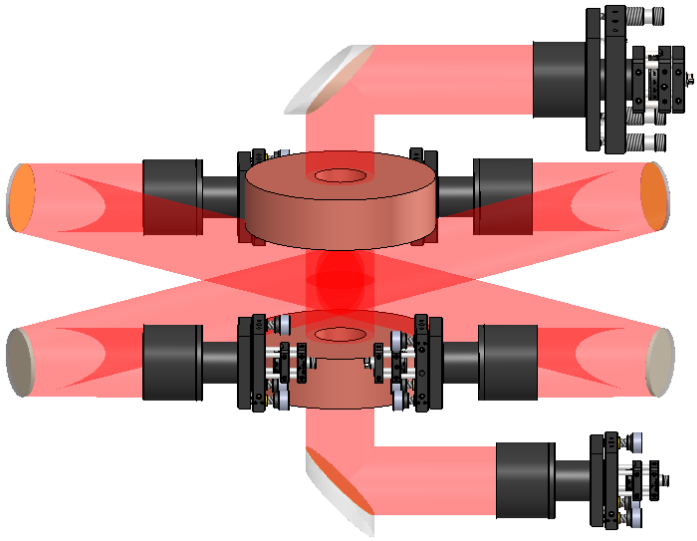

Figure 2.2: **A 3D CAD drawing of the MOT, with light delivered through optical fibers.** Each MOT beam has a steering mirror to account for all degrees of freedom. The optics for the beam coming from above are modified to accommodate the cage system for the 50 mm elliptical mirror. The quadrupole trap coils translate from the MOT to the science side along a linear translator (not shown). A detailed exploded view of the MOT fiber launch is shown in Fig. 2.3. [32, 33]

define the horizontal plane, with $\hat{\mathbf{y}}$ along the long axis of the vacuum chamber. A dc electromagnetic coil in an anti-Helmholtz configuration provides a spherical quadrupole field of 10 G/cm along $\hat{\mathbf{z}}$, which is the direction of symmetry of the coils. Three counter-propagating lasers, 20 MHz red-detuned from the $|5^2S_{1/2}F = 2\rangle \rightarrow |5^2P_{3/2}F' = 3\rangle$ cooling transition provide Doppler cooling to atoms near the trap center. The magnetic field strength increases linearly away from the field zero, which produces a spatially-dependent Zeeman shift to the atomic energy levels. The combination of the laser fields and the quadrupole field provide confinement. A 3D CAD drawing of the MOT is shown in Fig. 2.2.

The output of the TA is coupled into the MOT AOM, which deflects the laser into the fibers delivering light to the six MOT beams. With the MOT AOM turned off, the

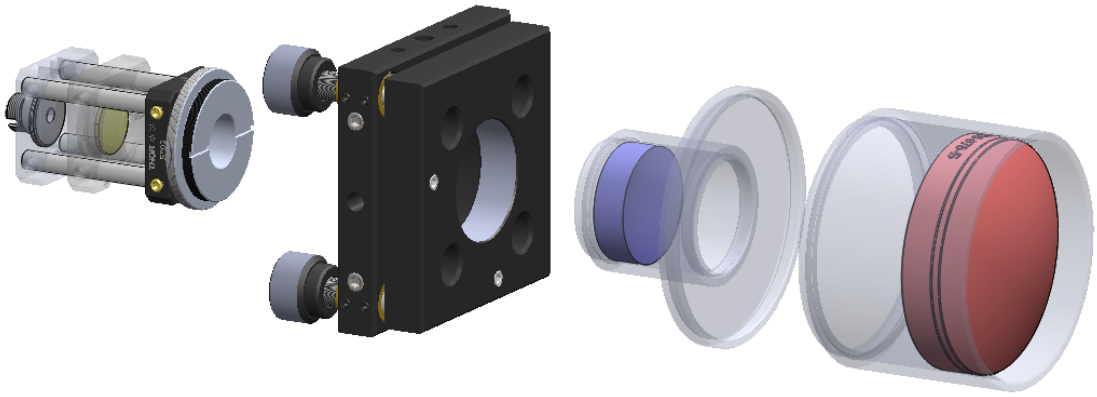

Figure 2.3: **An exploded view of the MOT fiber launch optics.** From left to right: An optical fiber is launched in a 16 mm cage system. A zero-order quarter-wave plate (yellow) is mounted in a rotation mount to change the polarization from linear to circular. A lens tube adapter connects the cage to the threaded tip-tilt mount. The light passes through ⌀25 mm $f = -25$ mm bi-concave lens (blue) to shorten the overall length of the system. The light is collimated with a ⌀25 mm $f = 75$ mm doublet (red). A profile of the collimated beam waist is shown in Fig. 2.4 [32–34].

TA light is sent instead to the pump and probe optics, which are described later on. The MOT light is split into three beams using half-wave plates and polarizing beam splitters (PBSs). Each beam is fiber coupled into a 1×2 polarization maintaining fiber (Thorlabs PN780R5A1). The outputs of each pair face one another at the MOT. The output collimation package is pictured in Fig. 2.3. After leaving the fiber adapter, MOT light passes through a quarter-wave plate to make the requisite circularly-polarized light. The beam passes through a telescope to collimate the light with a $1/e$ beam waist of 19 mm, as shown in a 1D profile in Fig. 2.4. The system is mounted to a tip-tilt kinematic mount for adjustment.

The MOT shutter needs to have a relatively fast closing time because leakage light through the MOT AOM can spoil optical pumping. We use a Uniblitz LS2, which is positioned near the focus of the MOT light before it is split and coupled into the three optical fibers. The closing time is about 1 ms. A home-built shutter with a 5 ms

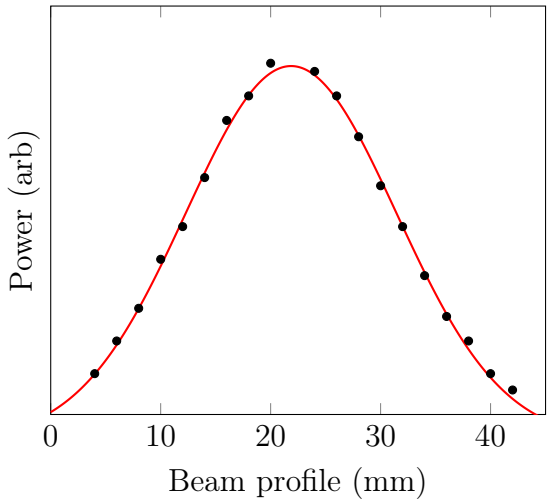

Figure 2.4: **A 1D profile of a MOT beam collimated out of the fiber.** Data are taken using the razor blade method to find the error function, from which the beam's profile is extracted [35]. The $1/e$ beam waist $w = 19$ mm.

closing time is also included in the beam path further upstream, before the light leaves the laser box. In the older setup, this slower shutter was the only MOT shutter. The increase in MOT light intensity spoils optical pumping, so a faster shutter is needed. Both shutters remain in use and are turned on or off together, with the slower shutter eliminating the possibility of stray light scattering off of optics outside the laser box.

A photodiode is set up to measure the fluorescent light scattered by atoms in the MOT, giving us a rough estimation of the atom number. The photodiode is also used for testing the performance of the MOT and subsequent experimental steps. Finally, the photodiode can be used to trigger the start of the experiment, such that each time the experiment begins with roughly the same number of atoms. A microcontroller repeatedly measures the voltage on the photodiode, and cues the computer when to start the experiment. A temporary switch can be used to reset the acceptable MOT level to 90% of its current value, and the interlock can be overridden if the user prefers a set time between runs.

2.1.3 Transfer to the magnetic trap

The MOT reaches a steady state after roughly 10 seconds with about 2×10^9 atoms, at which point the atoms are transferred to the magnetic quadrupole trap. The subsequent experimental sequence is given in Appendices A.2.1 and A.2.2. First, the cooling laser is detuned 60 MHz further red from the transition line, allowing photons to penetrate further into the cloud and making the volume smaller, forming a compressed MOT (CMOT). The magnetic field is then turned off and the atoms undergo an 8 ms optical molasses phase, which reduces the temperature of the atoms further. A full discussion of polarization gradient cooling can be found in Dalibard [36]. The performance of the optical molasses phase can be characterized with the MOT photodiode by measuring the decay time, i.e. measuring the fluorescence from atoms leaving the MOT after turning off the magnetic field. If the beam intensity balance is poor or there is a background magnetic field, then atoms are pushed more quickly from the region near the magnetic trap center. We have found the molasses easier to optimize with the beams fiber coupled, likely because the spatial mode of the fibered beams is better. A better spatial mode means the molasses beams are more uniform over the capture volume, reducing unwanted forces from gradients in the laser intensity. The beam balance between each counter-propagating pair is not adjustable, but all fiber splitters were measured to have outputs within the 7% margin of error specified by the manufacturer. The beam balance between the pairs can be adjusted on the inputs using the half-wave plates controlling the transmission through each PBS. These should be adjusted while measuring the power transmission through two different fibers, and should agree to within 5%. With the photodiode, we measure $1/e$ molasses decay times of 1 second with the fiber MOT; the old laser setup typically

had decay times around 250 ms.

After cooling to this point, the atoms are in different Zeeman sub-levels of the $|5^2S_{1/2}, F = 2\rangle$ ground state. We require atoms in the $|F = 2, m_F = 2\rangle$ ground state for the magnetic trap. To pump atoms into this state, we apply σ_+ light to the atoms to impart angular momentum. The light is tuned to the $F = 2 \rightarrow F' = 2$ transition, which is roughly 267 MHz redder than the cooling transition. To create the σ_+ light, a circularly polarized pump beam with intensity 8 mW/cm^2 is incident on the MOT along $\hat{\mathbf{y}}$, concentric with a bias coil near the MOT. The pump light is switched on using an 80 MHz AOM. As shown in Fig. 2.1, we use the second-order output beam from the AOM. The bias coil is switched on 2 ms before the pump AOM is activated, and both remain on for 500 μs. Selection rules require the atoms absorbing a photon from the laser to change m_F by +1. The atoms return to the ground state with m_F unchanged, or ±1. After several cycles, atoms begin building up in the $|F = 2, m_F = 2\rangle$ sub-level, which is dark to the σ_+ light. During this optical pumping phase, the MOT light is turned off.

After the atoms have undergone optical pumping, they are loaded into the magnetic quadrupole trap. The atoms are trapped via the Zeeman shift, i.e. $U = -\boldsymbol{\mu} \cdot \mathbf{B}$, where $\boldsymbol{\mu}$ is the atom's magnetic moment and $\mathbf{B}$ is the applied magnetic field. The energy depends on the amplitude of the magnetic field,

$$U = g_F \mu_B m_F |\mathbf{B}|, \tag{2.1}$$

where $g_F = 2$ is the Landé g-factor for the given state.

The magnetic coils are turned on to roughly 60 G/cm for 40 ms before being

ramped up to 388 G/cm over 200 ms to limit heating, which can cause atom losses. We can measure the efficiency of the transfer to the magnetic trap using the MOT photodiode by loading the trap and then flashing on MOT light for 50 ms. The photodiode measures both the original MOT level and the signal from successfully trapped atoms. We typically require at least 40% of the atoms in the MOT be transferred to the magnetic trap to make a condensate. At this efficiency, there are about 10^9 atoms at about 1 mK in the tight magnetic trap.

2.1.4 Evaporative cooling

Once the atoms are in the magnetic trap, the coils are mechanically transported 500 mm along $\hat{\mathbf{y}}$ from the MOT vacuum chamber to the science vacuum chamber. To lower the temperature of the system further, we use radio frequency (RF) evaporation. A circular antenna with a 10 mm diameter is positioned around 5 mm from the atoms. The RF field drives a transition with $\Delta m_F = -1$, as shown in Fig. 2.5. The field is ramped down from $\omega = 2\pi \times 90$ MHz. The hottest atoms in the trap will absorb the higher frequency photons because they are able to move further from the trap center and thus experience the largest Zeeman shift. With each scattered RF photon, hotter atoms can transition to uptrapped or anti-trapped Zeeman states. As hotter atoms leave the trap, the remaining trapped atoms rethermalize and the sample's temperature is decreased. The RF frequency is exponentially decreased with a 12-s time constant, which roughly matches the rethermalization rate.

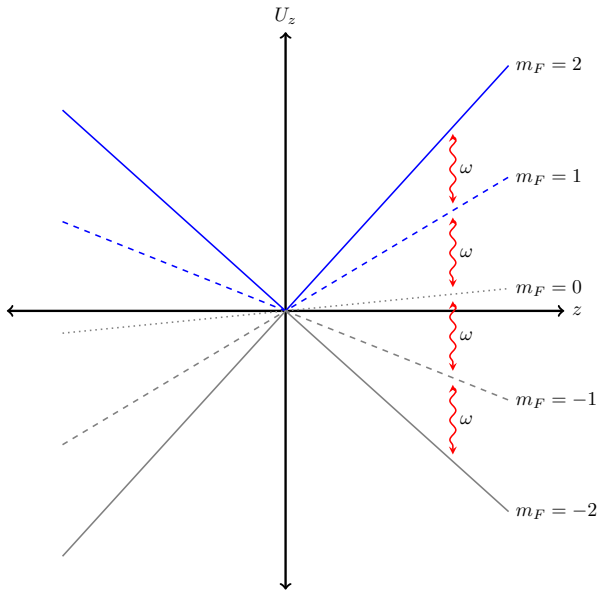

Figure 2.5: **Evaporative cooling in the dc quadrupole trap.** The quadrupole trap can hold m_F = 1 and m_F = 2 atoms, shown here in blue. RF photons with frequency ω are couple the sub-levels, with energy spacing 0.7 MHz/Gauss. Gravity is included here, making the potential asymmetric along $\hat{\mathbf{z}}$, with a field gradient of approximately 10 Gauss/cm. Figure from [29].

2.1.5 The TOP Trap

There is a limit to how cold the atoms can get in the quadrupole trap. As atoms get colder, they have less energy and therefore spend more time near the center of the trap, where the magnetic field is zero, as shown along $\hat{\mathbf{z}}$ in Fig. 2.5. As an atom passes through the field zero of the trap, it can reorient its spin state and become untrapped, in what is called a Majorana loss [37]. The colder the atoms get, the larger the loss rate becomes. There are several methods to avoid Majorana losses and continue to reduce the energy of the ensemble in order to make a BEC. In our experiment, we add a rotating magnetic bias field, which moves the field zero around the atoms faster than they are able to follow, but not so fast that the atomic spins lose their alignment to the field. This is called a time-orbiting potential (TOP) trap [38].

The TOP trap uses the dc quadrupole field described earlier, which is generated by two coils such that

$$\mathbf{B}_{\mathrm{dc}} = B'_{\mathrm{dc}}\left(\frac{1}{2}x\,\hat{\mathbf{x}} + \frac{1}{2}y\,\hat{\mathbf{y}} - z\,\hat{\mathbf{z}}\right), \tag{2.2}$$

where B'_{dc} is the field gradient and $\hat{\mathbf{z}}$ points up. In the simplest configuration, the additional bias field rotates the field zero around the atoms in a circle in the horizontal plane. In our implementation, the bias field rotates on a sphere. This will be useful for our subsequent atom interferometry experiments. The bias field rotates along the longitude lines of a sphere at Ω_1, with the plane of rotation precessing at a frequency Ω_2. Mathematically, the bias field is given by

$$\mathbf{B}_{\mathrm{bias}} = B_0\Big[\sin(\Omega_1 t)\cos(\Omega_2 t)\,\hat{\mathbf{x}} + \sin(\Omega_1 t)\sin(\Omega_2 t)\,\hat{\mathbf{y}} + \cos(\Omega_1 t)\,\hat{\mathbf{z}}\Big]. \tag{2.3}$$

Again, the atoms are trapped by the Zeeman effect as they were in the quadrupole trap, with a potential energy $U = -\boldsymbol{\mu}\cdot\mathbf{B}$. With the field rotating fast enough, the atoms experience the time average of the potential, so

$$U = g_f m_F \mu_B \langle|\mathbf{B}|\rangle. \tag{2.4}$$

The time average of the total magnetic field is simple to calculate as a second-order Taylor expansion, and gives the total potential in the TOP trap

$$U_{\mathrm{tot}} = \mu_0 B_0 + mgz + \frac{1}{2}m\omega_0^2 x^2 + \frac{1}{2}m\omega_0^2 y^2 + \frac{1}{2}m\omega_z^2 z^2, \tag{2.5}$$

where the horizontal trap frequencies are

$$\omega_0 = \left[\frac{2\mu_B}{m}\left(\frac{3}{32}\frac{B'^2_{\mathrm{dc}}}{B_0}\right)\right]^{1/2} \tag{2.6}$$

and the vertical trap frequency is

$$\omega_z = \left[\frac{2\mu_B}{m}\left(\frac{1}{4}\frac{B_{\rm dc}'^2}{B_0}\right)\right]^{1/2}. \tag{2.7}$$

After the preliminary stage of RF evaporation in the quadrupole trap, the atoms are put into the TOP trap by quickly turning on the bias field at full strength, 23 G. At this point, we are able to continue evaporative cooling using the field zero of the TOP trap to expel the hottest atoms in the system. By reducing the strength of the bias fields, the magnetic field zero can be moved closer to the center of the trap. More energetic atoms will be able to move the furthest from the center and will encounter the field zero and become untrapped through Majorana loss. The strength of the bias field is ramped from 23 G to 7 G over nine seconds. This reduces the temperature of the cloud further, and also increases the TOP trap frequencies. After a second RF sweep from 30 MHz to 4.3 MHz over 12 seconds, the condensate is formed.

After producing the BEC, it is subsequently transferred to a purely ac TOP trap, or "waveguide," which is described in detail in Chapter 3. Transferring the condensate is simple: an ac quadrupole field is ramped on while the dc quadrupole field is ramped off over the course of nine seconds. As with any adiabatic process, this handoff has to be done smoothly to avoid adding energy to the system. The centers of the dc TOP trap and the waveguide are not automatically coincident since the fields are produced from different coils. Therefore loading the atoms into the waveguide can result in excitations in the form of residual oscillations, which is problematic for AI applications. A step-by-step optimization of the transfer process is required to ensure each segment of the ramp is long enough to minimize residual oscillations. The experimental sequence is provided in Appendix A.2.5.

2.1.6 Imaging

The last step of each experiment is imaging. We use absorption imaging, where an on-resonant laser is directed onto the condensate. Multiple images are needed for each measurement. First, the condensate absorbs laser light, causing a shadow on the camera's CCD in the "atoms image." The absorbed light heats the atoms, causing the destruction of the condensate. A second "no atoms" image is taken shortly after this, which has only the probe laser light. After subtracting background light (a third image taken without probe light) from both images, they are mathematically divided giving the final divided image,

$$\text{divided} = \frac{\text{atoms} - \text{background}}{\text{no atoms} - \text{background}}, \tag{2.8}$$

providing images such as those in Fig. 2.6. Two cameras are set up to image the xy plane from above, and the yz plane from the side.

Because absorption imaging requires multiple images, the divided image can be noisy. If the probe beam drifts, or there are vibrations in the imaging optics, that introduces noise into the divided image. If the probe beam has an unstable Poynting vector, that can cause erroneous absorption in the divided image. This sort of effect can occur if the beam free space propagates over a long path, but can easily be solved with the addition of an optical fiber. Mechanical vibrations, i.e. from the camera's shutter opening and closing, also add noise. Small changes in the camera optics cause the probe beam to move on the CCD, resulting in what looks like diffraction in the divided image. An optomechanical consideration for the xy (top) camera is that the camera optics all need to be fixed above the vacuum chamber. In previous versions of

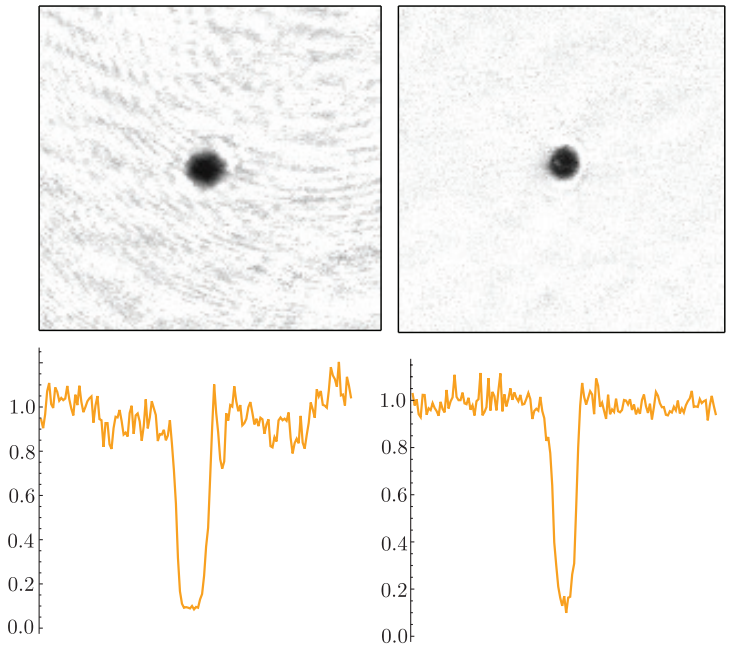

Figure 2.6: **Absorption images of a condensate and associated x profiles.** The left use the static imaging technique, and the right use the kinetic imaging technique. Kinetics imaging has an improved pixel noise value to four times lower than statics.

this experiment, the camera optics were put together in a 16 mm cage system, which was mounted to the optics table with a ⌀1.5" post. To improve the system's stability, all of the imaging optics were moved to a breadboard mounted 10" above the optics table, which is less susceptible to vibrations.

The new top camera imaging system is shown in Fig. 2.7. The system magnifies the image of the condensate twice. A pair of lenses magnifies the primary image by a factor of 2, then a microscope objective makes an image on the camera with 2.5× magnification. The first telescope is needed to provide a large working distance with the lenses we use, which allows us to easily focus the final image onto the camera. The microscope objective (Mitutoyo MY5X-802) provides further magnification with low aberrations, and has the added advantage of being easily interchangeable if we prefer a different field of view. With two telescopes, there are two imaging planes: the

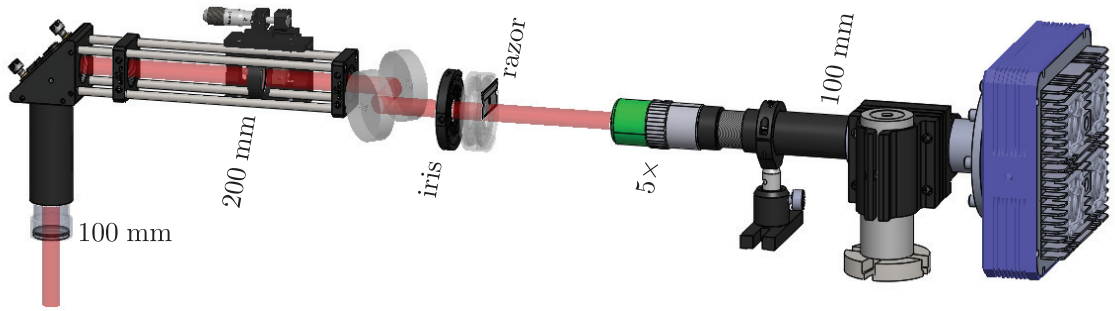

Figure 2.7: **A 3D CAD rendering of the updated top camera imaging optics, with kinetics imaging.** The path of the probe beam and image is shown in red. To help reduce vibrations, a lens tube clamp was added to the camera's lens tube. The imaging system is mounted to a $12'' \times 36''$ breadboard. Some optical mounts were omitted for simplicity. A CAD drawing of the camera (Apogee Alta U6) provided by Andor. [32, 33]

primary plane located 34 mm from the front of the microscope objective, the working distance of the objective, and the secondary plane on the CCD.

The top probe beam propagates upwards into a ⌀25 mm, f = 100 mm achromatic collection lens. After reflecting off of a cage-mounted mirror, the image propagates parallel to the table to the ⌀25 mm, f = 200 mm collimation lens, which is in a cage-mounted translation stage (Thorlabs CT1). A pair of ⌀50 mm dielectric mirrors enable the image to be centered on the CCD. An iris is located near the primary imaging plane to clip the probe beam, preventing it from scattering off of the lens tubes downstream. The 5× microscope objective and a f = 200 mm achromatic lens inside the lens tube make the second telescope, imaging the condensate onto the CCD. The lens tube connected to the camera is clamped to the breadboard to reduce vibrations from the camera shutter opening and closing.

The quality of an absorption image can be degraded because two separate images are used in each shot because the probe beam is non-uniform and can change in time. The time between the two pictures can cause noise in the divided image, which

is limited by the time to transfer the image from the camera to the computer. In previous experiments, the two frames needed for each image were taken over 4 seconds apart. This led to significant diffraction and blurring in the divided image. Ideally, the time between these two images should be on the order of a few milliseconds, just long enough for the atoms in the first image to be eliminated from the second so those atoms do not contribute to the "no atoms" image. To get closer to this target, we switched to a "kinetics" imaging scheme. The top half of the CCD is blocked, using a razor blade mounted near the primary imaging plane. The first image is taken on the bottom half of the CCD, and is then translated up to the top half of the CCD. The second image is taken 100 ms later, again, on the bottom half. After the image is downloaded, the background is subtracted and the two images are divided to make a final image. This technique was adapted from previous work by Leonard [39].

The improvement over the old "static" imaging system used before is significant. To compare them, a representative square region of the divided images not containing the condensate was analyzed. The standard deviation over that region was measured statistically using ImageJ [40], σ, and was then divided by the typical area of a condensate to get a measure of how accurately condensate number can be determined,

$$\sigma_c = \frac{\sigma}{w_x\, w_y}, \tag{2.9}$$

where w_x and w_y are the waists of the condensate along the two axes of the camera. A typical static image had pixel value noise $\sigma_c = 0.086$, which is reduced to $\sigma_c = 0.02$ with kinetics imaging. A comparison between the old imaging technique and our new kinetics imaging with more stable optics is shown in Fig. 2.6.

The yz (side) camera is a similar optical setup to the top camera's. Fortunately,

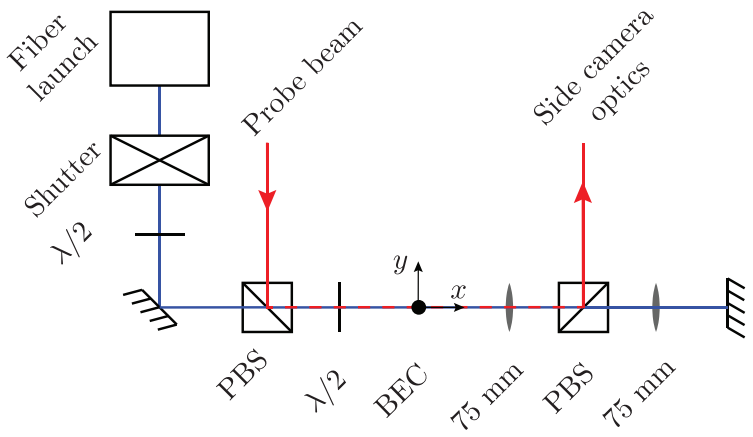

Figure 2.8: **Block diagram of the side imaging and x Bragg beam sharing an axis.** The Bragg beam, shown in blue, is launched from an optical fiber. The probe beam, shown in red, is launched from an independent fiber and some upstream optics are not shown here, for simplicity. The two beams are joined on a PBS. The following half-wave plate sends the probe light to the camera and the Bragg light to the retro-reflecting mirror, and can be used to send the Bragg laser to the side camera for alignment. The first 75 mm achromatic lens is the collection lens of the imaging system. The second 75 mm lens in the Bragg beam path serves to keep the beam collimated in a $1:1$ telescope.

this camera system need not meet the same noise requirements as the top camera because it is not used for any AI measurements. It is used in this system to help to optimize BEC production, transferring the condensate from the dc trap to the waveguide, and can be used to measure the cloud's temperature. The system is similar to the top camera's with two telescope pairs, the first with ⌀25 mm doublet lenses (f_1 = 75 mm and f_2 = 300 mm), and the second combines a 2× microscope objective with a ⌀25 mm doublet lens (f = 100 mm). Several steering mirrors are included to direct the image onto the CCD.

The complication comes into the side camera's imaging optics because it shares an optical axis with the x Bragg beam. Combining the two beams efficiently requires

polarizing optics. Since optical fibers are used in this setup, the polarizing optics can introduce power drifts, so care must be taken to stabilize the beams' polarization states. A block diagram of the optical system is shown in Fig. 2.8. The probe beam and Bragg beam are joined on the output of a PBS, making their polarization states perpendicular to one another. A half-wave plate is included to direct the Bragg beam either to the side camera or to the retro-reflecting mirror. With the light directed onto the CCD, we are able to take an image of the laser and ensure the laser is incident on the atoms. After propagating through the vacuum chamber and being absorbed, probe light passes through the 75 mm collection lens before being reflected through another PBS, which directs the image and probe light to the subsequent side camera optics. A second 75 mm lens in the Bragg beam path is needed to collimate the Bragg laser in a $1:1$ telescope.

2.2 Bragg Splitting

Like optical interferometers, matter-wave interferometers require reliable methods for splitting a coherent wave and then recombining it on the output. For optical systems, it is easy enough to understand how beamsplitters and mirrors operate. These are trickier both conceptually and in practice with matter-waves. In our experiment, it requires the brief application of the Bragg laser, an off-resonant standing wave, which creates two counter-propagating condensates traveling along the direction of the Bragg laser field [41, 42].

An atom in a standing laser field is able to absorb a photon from the field coming from the left, and be stimulated to emit a photon into the field coming from the right.

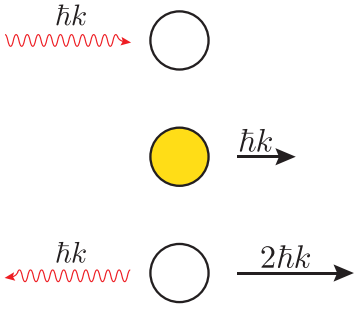

Figure 2.9: **A cartoon of Bragg scattering.** From top to bottom, an atom initially at rest absorbs a photon from the field incident from the left. The atom moves to a virtual excited state (yellow), picking up a momentum kick $\hbar k$. The atom emits a photon into the field incident from the right, moving back to the ground state, with another momentum kick to the right.

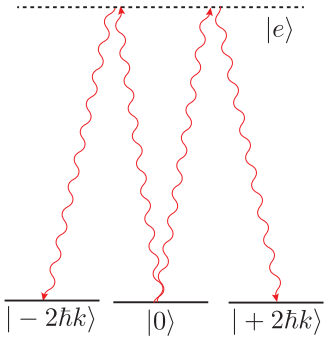

Figure 2.10: **An energy diagram of Bragg scattering.** An off-resonant standing wave is applied to atoms starting in the rest state, $|0\rangle$. Atoms absorb from one beam and emit into the other, changing their momentum by $\pm 2\hbar k$. In this two-photon transition, atoms move through a virtual excited state, $|e\rangle$.

Each photon imparts momentum $\hbar k$ onto the atom, so the atom travels to the right with momentum $2\hbar k$ after this process. The opposite is equally likely, resulting in the atom traveling left with the same momentum. As a result, we observe two wave packets traveling away from each other, each with $2\hbar k$ momentum, which we typically express in terms of the Bragg velocity kick $v_B = 2\hbar k/m$, or about 12 mm/s. Higher momentum kicks are also possible by increasing the intensity of the Bragg light. We use $4\hbar k$ kicks in some of the work described in Chapter 3.

The Bragg laser used for the work in this thesis was a home-built diode laser, not to be confused with the new Vescent laser described earlier in this chapter. The laser operates around 780.233 nm without frequency stabilization. An 80 MHz AOM is used to switch the laser on quickly, on the order of 50 ns. There are two Bragg

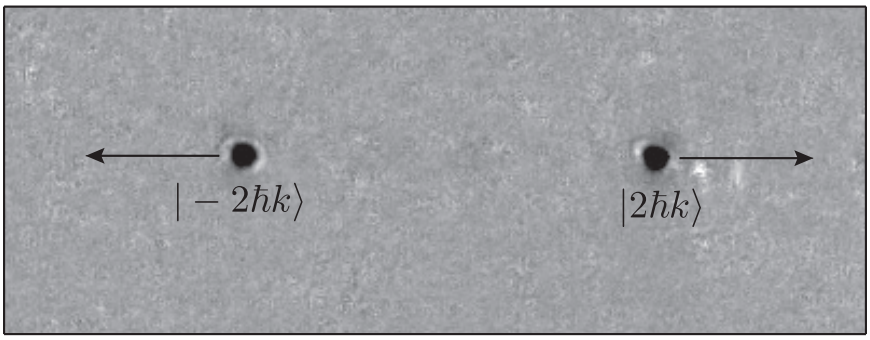

Figure 2.11: **A Bragg split along x.** The condensate is split into a superposition of momentum states $|\pm 2\hbar k\rangle$. The motion of each wave packet is roughly sinusoidal because the atoms are confined in a nominally harmonic trap. The size of each cloud is about 15 μm. This image was taken 20 ms after the Bragg split was applied.

beams, one aligned along $\hat{\mathbf{x}}$ and the other along $\hat{\mathbf{y}}$. Each Bragg beam is delivered to the experiment through an optical fiber, and their beam paths can be adjusted with a 2-axis translation stage and a tip-tilt steering mirror, each with micrometer adjusters. Each beam is retro-reflected back into the fiber to create a well-aligned standing wave. The beam paths are shown in a 3D CAD model of the experiment in Fig. 2.13. The beams are independently shuttered such that each can be applied to the atoms independently. The x Bragg beam has a larger waist than the y Bragg beam in order to split two clouds separated by almost 0.5 mm, which is discussed in Chapter 4.

Both Bragg beams have their share of optomechanical challenges. The x Bragg beam's arise because it shares an optical axis with the side camera's probe beam, which is explained in the previous section and illustrated in Fig. 2.8. The drawback is the introduction of polarizing optics. If the output polarization of the optical fiber is unstable, the transmission through the PBS upstream of the condensate is unstable and subject to drift, which is problematic for consistent splitting operations. Careful alignment of the input polarization to the optical fiber is necessary to keep the power

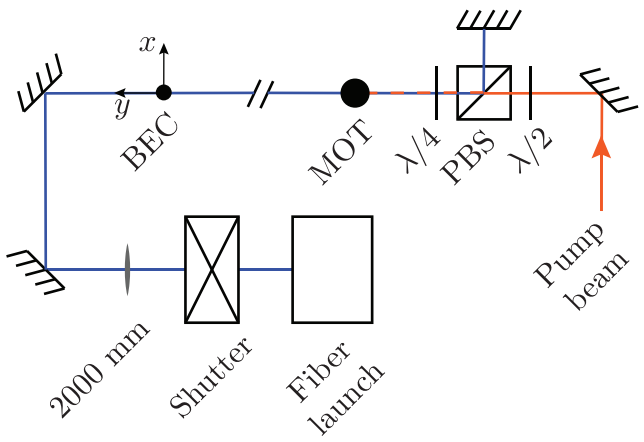

Figure 2.12: **Block diagram of the y Bragg beam and pump optics sharing an axis.** The Bragg beam, shown in blue, is launched from an optical fiber. The beam propagates through the long axis of the chamber, which is 4' long. Because of the polarization requirements of the pump beam, the y Bragg beam propagates through a quarter-wave plate and PBS, so it loses half its power. The 2000 mm lens in the Bragg beam path gently focuses the y Bragg beam, so the retro-reflected beam remains roughly collimated at the condensate. The half-wave plate in the pump beam acts as modulation along with the PBS.

through the PBS stable.

The y Bragg beam has a different set of challenges, as it propagates up the vacuum chamber and is retro-reflected near the pump optics. As shown in Fig. 2.12, the Bragg beam shares an optical axis with the pump laser. On the MOT side where the pump beam enters the vacuum, a PBS separates the Bragg laser and sends it to the retro-reflecting mirror. A quarter-wave plate is required to make the pump light circular, while the Bragg polarization must be linear. Consequently, the Bragg laser loses half its power as it passes through the PBS.

Coarse alignment of the Bragg beams is simple. After producing a condensate, the Bragg beam is applied with the retro mirror blocked for 10 ms, which is much longer than in the splitting operation. If the beam is partially incident on the condensate, the atoms will absorb light and the subsequent absorption image will have a degraded

absorption signal. The Bragg launch translation stage is then adjusted until the condensate is completely destroyed by the Bragg beam, and then repeated to more precisely align the beam with Bragg pulses of 1 ms. If coarse alignment proves difficult, the Bragg detuning can be reduced to scatter more photons. Once the beam is sufficiently aligned on the condensate, the retro mirror is unblocked. The retro mirror is adjusted until light propagates back through the optical fiber, ensuring the best overlap in the standing wave. This gives us a starting point for work discussed in the next chapters, which requires very precise alignment of the Bragg beams along the principle axes of the trap.

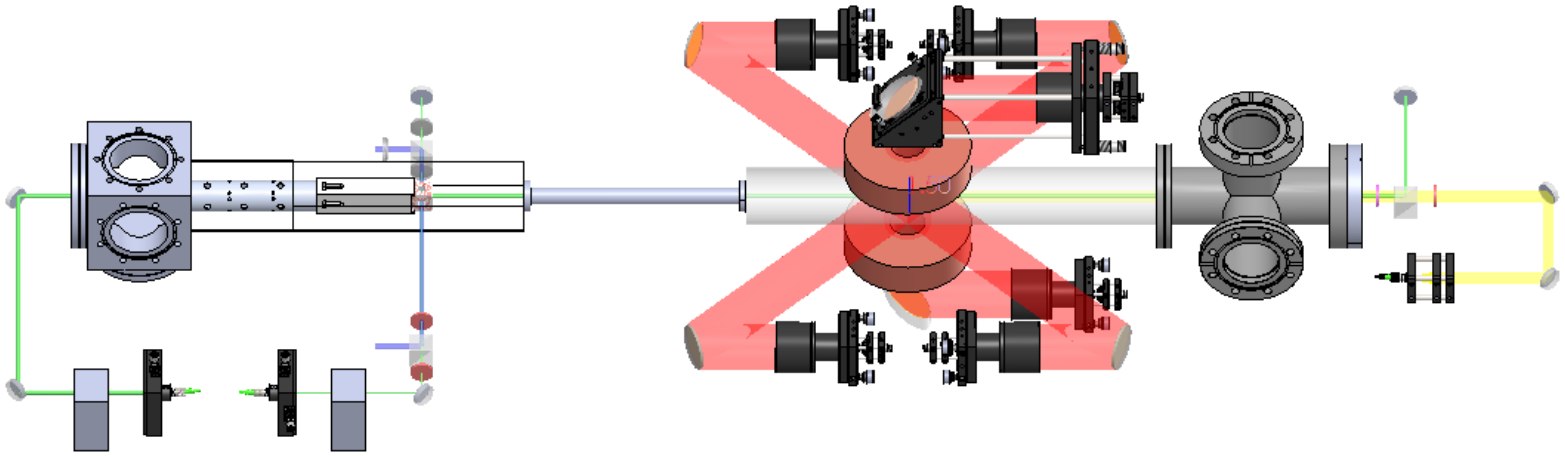

Figure 2.13: **A 3D rendering of the vacuum system.** Atoms from the MOT on the right are transferred to the science side to make a BEC within the waveguide cube. The Bragg beams are shown in green, starting at fiber collimators in the bottom left before passing through shutters. The x Bragg beam points across the chamber, and the y Bragg beam propagates the length of the vacuum chamber. The side camera's probe beam is shown in blue, the pump beam is shown in yellow, and wave plates are shown in pink. The y Bragg beam shares access with the pump beam. To accommodate the circularly polarized pump light, the y Bragg beam has to pass through a $\lambda/4$ wave plate twice, reducing the power by half.

3 The magnetic waveguide

In order to build a trapped-atom Sagnac interferometer, we need a stable and tunable trap. With a clearer picture of the potential, $U(\mathbf{r})$, we are able to make adjustments such that the atoms propagate in closed loops during interferometer measurements. Because we know the coil geometry and are able to measure the currents producing the trapping fields, we can learn about the potential through analytical analysis. That gives us information about the influence of higher-order terms, as well as trap inhomogeneities.

We are also able to use the atoms themselves to learn about the trap. Using the Bragg beams, we can split the atoms and allow them to oscillate freely along x and y. We can also induce oscillations along z by making rapid non-adiabatic changes to the trapping fields. These tests allow us to monitor the trajectories of the atoms as they move through the trap. We can treat the center-of-mass motion of the condensate as classical, so if we have an accurate picture of $\mathbf{r}(t)$, we can easily find the acceleration $\mathbf{a}(t)$. This is directly proportional to the force, and from there the potential can be determined by integration. This last step is likely to produce large errors, so we instead use a model of the potential and find the best fit of the trajectories.

3.1 Time-orbiting potential trap

First, we can calculate the potential based on the coil geometry. This helps us understand the data further down the road, and paints a picture of the impact non-idealities have on the atoms trajectory when we try to make an interferometer. The principle of the TOP trap is to combine a spherical quadrupole magnetic field with a rotating bias magnetic field such that the zero of the quadrupole is displaced and orbits around the trap center. The rotation rate is fast compared to the motional frequency of the atoms, but slow compared to the Larmor frequency of the atomic spins. The atoms therefore maintain their spin state and experience a time-averaged potential $U = -\mu \langle |\mathbf{B}| \rangle$, where μ is the magnetic moment of the spin state. Our implementation has a few special features [43]. First, the quadrupole field oscillates synchronously with the bias rotation, which generates a constant force at the trap center. We set this force to cancel gravity. Second, our bias field rotates in three dimensions, which allows us to better control the symmetry of the trap.

In the simplest case, the bias field has the form

$$\mathbf{B}_0 = B_0 \left(\cos \Omega_1 t \cos \Omega_2 \, \hat{\mathbf{x}} + \cos \Omega_1 t \sin \Omega_2 t \, \hat{\mathbf{y}} + \sin \Omega_1 t \, \hat{\mathbf{z}} \right), \tag{3.1}$$

which traces over the surface of a sphere. The frequencies Ω_1 and Ω_2 are nominally incommensurate. The quadrupole is

$$\mathbf{B}_q = -B_1' \left(-\frac{1}{2} x \, \hat{\mathbf{x}} - \frac{1}{2} y \, \hat{\mathbf{y}} + z \, \hat{\mathbf{z}} \right) \sin \Omega_1 t. \tag{3.2}$$

The time-dependent amplitude of the field is given by

$$|B|(t) = \sqrt{B_x^2 + B_y^2 + B_z^2}, \tag{3.3}$$

or

$$|B|(t) = B_0\Bigg[1 + \frac{1}{2}\kappa x \sin(2\Omega_1 t)\cos\Omega_2 t + \frac{1}{2}\kappa y \sin(2\Omega_1 t)\sin\Omega_2 t - 2\kappa z \sin^2\Omega_1 t + \frac{1}{4}\kappa^2\left(\rho^2 + 4z^2\right)\sin^2\Omega_1 t\Bigg]^{1/2} \tag{3.4}$$

for $\kappa \equiv B_1'/B_0$ and $\rho^2 = x^2 + y^2$. The field oscillates faster than the atoms can follow, so we consider the time average of the field,

$$\langle f(t)\rangle = \lim_{T\to\infty}\frac{1}{T}\int_0^T f(t)\,\mathrm{d}t. \tag{3.5}$$

To evaluate the integral, we can Taylor expand Eq. (3.4) in the small dimensionless quantities $(\kappa x, \kappa y, \kappa z)$ using the Taylor approximation for $\epsilon \ll 1$,

$$\sqrt{1+\epsilon} \approx 1 + \frac{1}{2}\epsilon - \frac{1}{8}\epsilon^2 + \frac{1}{16}\epsilon^3 - \frac{5}{128}\epsilon^4 + \ldots \tag{3.6}$$

Terms up to fourth order are included, and we find the time-averaged magnetic field to be

$$\langle|B|\rangle = B_0\Bigg[1 - \frac{1}{2}\kappa z + \frac{7}{128}\kappa^2\rho^2 + \frac{1}{16}\kappa^2 z^2 + \frac{1}{32}\kappa^3 z^3 + \frac{9}{256}\kappa^3\rho^2 z - \frac{237}{131072}\kappa^4\rho^4 + \frac{17}{1024}\kappa^4 z^4 + \frac{93}{4096}\kappa^4\rho^2 z^2\Bigg]. \tag{3.7}$$

Taking z vertical, the total potential in gravity g is $U = \mu\langle|B|\rangle + mgz$, and we set

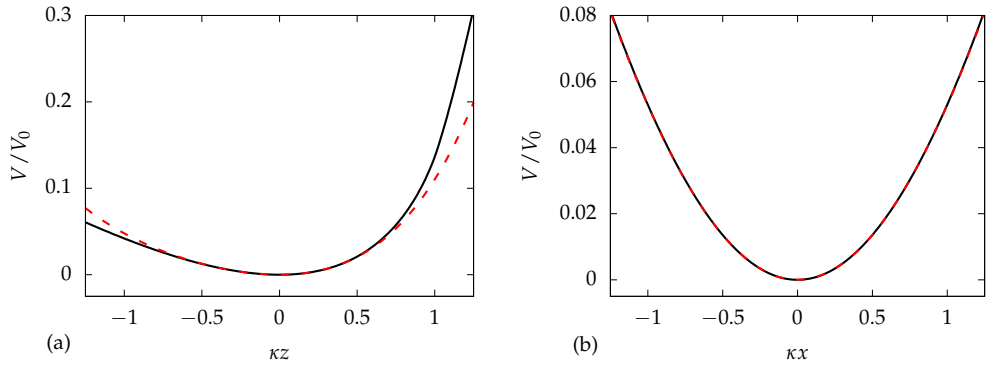

Figure 3.1: **The TOP trap potential, as a function of x and z.** Here $V_0 = m\omega_0^2/2\kappa^2 = (7/128)\mu B_0$. The solid black curve is an exact numerical calculation and the dashed red curve is the polynomial expansion of Eq. (3.8). In (b), the two curves are indistinguishable.

$\mu B_0 \kappa = 2mg$ to place the potential minimum at the origin. We can then express the potential as

$$U(\mathbf{r}) = m\omega_0^2\left[\frac{1}{2}\rho^2 + \frac{\lambda^2}{2}z^2 + \frac{1}{3}az^3 + \frac{1}{2}b\rho^2 z + \frac{1}{4}c\rho^4 + \frac{1}{4}fz^4 + \frac{1}{2}h\rho^2 z^2\right] \tag{3.8}$$

with horizontal frequency

$$\omega_0 = \left(\frac{7}{64}\frac{\mu}{m}\frac{B_1^2}{B_0}\right)^{1/2} \tag{3.9}$$

and

$$\lambda^2 = \frac{8}{7} \qquad a = \frac{6}{7}\kappa \qquad b = \frac{9}{14}\kappa$$
$$c = -\frac{237}{3584}\kappa^2 \qquad f = \frac{17}{28}\kappa^2 \qquad h = \frac{93}{224}\kappa^2. \tag{3.10}$$

Clearly this potential is non-harmonic. The length scale $1/\kappa = B_0/B_1 \approx 0.6$ mm^{-1} also defines the size of the trap, since atoms with $\kappa z > 1$ will encounter the moving magnetic field zero and be ejected by Majorana spin flips [37]. Figure 3.1 compares this fourth-order expansion to a calculated time average of Eq. (3.4).

In reality, the bias field components will not be perfectly uniform and the gradient field will not be perfectly linear, and these variations will modify the trap potential. We address this point in the next section.

3.2 Field inhomogeneities

We suppose that each of the x, y, and z bias field components is established by a set of coils aligned to the corresponding axis and symmetric about the origin. The bias fields can be derived from a Legendre polynomial expansion of the magnetic scalar potential about the origin [44]. We consider a set of axial coils with cylindrical symmetry and finding the scalar potential's multipole expansion,

$$\psi = \sum_l A_l r^l P_l(\cos\theta). \tag{3.11}$$

For now, the coefficients A_l are considered arbitrary constants. With $z = r\cos\theta$ and $\rho^2 = x^2 + y^2 = r^2 - z^2$, the scalar potential to fourth-order is

$$\psi = A_0 + A_1 z + \frac{1}{2}A_2(2z^2 - \rho^2) + \frac{1}{2}A_3(2z^3 - 3\rho^2 z) + \frac{1}{8}A_4(8z^4 - 24\rho^2 z^2 + 3\rho^4). \tag{3.12}$$

The field from the coils is found by taking the gradient in Cartesian coordinates, $\mathbf{B} = \nabla\psi$, and relabeling the coefficients,

$$\begin{aligned}\mathbf{B} = {} & B_0\,\hat{\mathbf{z}} + B_1\left(z\,\hat{\mathbf{z}} - \frac{1}{2}x\,\hat{\mathbf{x}} - \frac{1}{2}y\,\hat{\mathbf{y}}\right) + B_2[(2z^2 - x^2 - y^2)\,\hat{\mathbf{z}} - 2xz\,\hat{\mathbf{x}} - 2yz\,\hat{\mathbf{y}}] \\ & + B_3\left[\left(z^2 - \frac{3}{2}x^2 - \frac{3}{2}y^2\right)z\,\hat{\mathbf{z}} - \frac{3}{2}\left(z^2 - \frac{1}{4}x^2 - \frac{1}{4}y^2\right)x\,\hat{\mathbf{x}} - \frac{3}{2}\left(z^2 - \frac{1}{4}x^2 - \frac{1}{4}y^2\right)y\,\hat{\mathbf{y}}\right].\end{aligned} \tag{3.13}$$

The trap is made up of three such coil pairs. The bias fields are even functions since they are produced by symmetric coil pairs, so the fields are

$$\mathbf{B}_x = B_0\Big[(1+\alpha)\sin(\Omega_1 t)\cos(\Omega_2 t+\beta)\Big]\Bigg(\hat{\mathbf{x}} + \gamma\left[\left(x^2 - \frac{1}{2}y^2 - \frac{1}{2}z^2\right)\hat{\mathbf{x}} - xy\,\hat{\mathbf{y}} - xz\,\hat{\mathbf{z}}\right] + \eta\left\{\left[x^4 - 3x^2(y^2+z^2) + \frac{3}{8}(y^2+z^2)^2\right]\hat{\mathbf{x}} + \left[\frac{3}{2}x(y^2+z^2) - 2x^3\right](y\,\hat{\mathbf{y}} + z\,\hat{\mathbf{z}})\right\}\Bigg), \tag{3.14}$$

$$\mathbf{B}_y = B_0\Big[(1-\alpha)\sin(\Omega_1 t)\sin(\Omega_2 t-\beta)\Big]\Bigg(\hat{\mathbf{y}} + \gamma\left[\left(y^2 - \frac{1}{2}x^2 - \frac{1}{2}z^2\right)\hat{\mathbf{x}} - xy\,\hat{\mathbf{x}} - yz\,\hat{\mathbf{z}}\right] + \eta\left\{\left[y^4 - 3y^2(x^2+z^2) + \frac{3}{8}(x^2+z^2)^2\right]\hat{\mathbf{y}} + \left[\frac{3}{2}y(x^2+z^2) - 2y^3\right](x\,\hat{\mathbf{x}} + z\,\hat{\mathbf{z}})\right\}\Bigg), \tag{3.15}$$

and

$$\mathbf{B}_z = B_0\Big[\cos(\Omega_1 t)\Big]\Bigg(\hat{\mathbf{z}} + \gamma\left[\left(z^2 - \frac{1}{2}x^2 - \frac{1}{2}y^2\right)\hat{\mathbf{z}} - xz\,\hat{\mathbf{x}} - yz\,\hat{\mathbf{y}}\right] + \eta\left\{\left[z^4 - 3z^2(x^2+y^2) + \frac{3}{8}(x^2+y^2)^2\right]\hat{\mathbf{z}} + \left[\frac{3}{2}z(x^2+y^2) - 2z^3\right](x\,\hat{\mathbf{x}} + y\,\hat{\mathbf{y}})\right\}\Bigg), \tag{3.16}$$

The constants γ, η are set by the coil geometry. We assume here that all the fields are produced by similar coils, but if not then we can introduce different parameters $(\gamma_x, \gamma_y, \gamma_z)$ and (η_x, η_y, η_z). The time-dependent terms include amplitude and phase adjustments, α and β. These are not set by geometry, but by the driving signals, and are easily adjustable parameters. The term α is an adjustment to the amplitudes of the horizontal bias fields, and the angle β is the phase between the horizontal

bias fields. These are both set by the function generators driving the coils. For the moment, we take $\alpha = \beta = 0$.

We take the quadrupole field to be cylindrically symmetric around the z axis, and antisymmetric along z. We can then obtain a general expansion from Eq. (3.13),

$$\mathbf{B}_q = \kappa B_0 \Bigg\{ z\,\hat{\mathbf{z}} - \frac{1}{2}x\,\hat{\mathbf{x}} - \frac{1}{2}y\,\hat{\mathbf{y}} + \xi\left[\left(z^2 - \frac{3}{2}x^2 - \frac{3}{2}y^2\right) z\,\hat{\mathbf{z}} - \frac{3}{2}\left(z^2 - \frac{1}{4}x^2 - \frac{1}{4}y^2\right)(x\,\hat{\mathbf{x}} + y\,\hat{\mathbf{y}})\right]\Bigg\}. \tag{3.17}$$

The constant ξ is again set purely by the coil geometry. Note that since the $\mathbf{B}_z$ and $\mathbf{B}_q$ fields have the same time dependence in Eqs. (3.16) and (3.2), the symmetric and antisymmetric components of Eqs. (3.16) and (3.17) can be combined to accommodate a non-symmetric geometry for the z coils.

If the various fields are produced by a circular current loop, the geometrical parameters can be obtained using the fourth-order Taylor expansion of the field from a loop along its axis. We take the loop radius to be a and the distance from the loop center to the coordinate origin to be s,

$$B(z) = \frac{\mu_0 I}{2a} \frac{1}{\left(1 + \frac{(z+s)^2}{a^2}\right)^{3/2}}. \tag{3.18}$$

Here I is the current and μ_0 is the permittivity of free space. We define $\zeta \equiv s/a$, and

expand in the parameter $u = (z/a)/(1+\zeta^2)$ to obtain

$$B(z) = \frac{\mu_0 I}{2a}\frac{1}{(1+\zeta^2)^{3/2}}\Bigg[1 - 3\zeta u + \frac{3}{2}\left(4\zeta^2 - 1\right)u^2 + \frac{5}{2}\zeta\left(3 - 4\zeta^2\right)u^3 + \frac{15}{8}\left(1 - 12\zeta^2 + 8\zeta^4\right)u^4\Bigg]. \quad (3.19)$$

Using this, we can read off the parameters

$$\gamma = \frac{3}{2a^2}\frac{4\zeta^2 - 1}{(1+\zeta^2)^2} \qquad \xi = \frac{5}{6a^2}\frac{4\zeta^2 - 3}{(1+\zeta^2)^2} \qquad \eta = \frac{15}{8a^4}\frac{1 - 12\zeta^2 + 8\zeta^4}{(1+\zeta^2)^4}. \quad (3.20)$$

In principle, an analytical polynomial expansion of the TOP trap potential such as in Eq. (3.8) could be calculated using the inhomogeneous fields of this section. We numerically calculate the potential at a given point $\mathbf{r}$ as

$$U(\mathbf{r}) = mgz + \frac{\mu}{\tau}\int_0^\tau \Big|\mathbf{B}_x \cos\Omega_1 t \cos\Omega_2 t + \mathbf{B}_y \cos\Omega_1 t \sin\Omega_2 t + (\mathbf{B}_z + \mathbf{B}_q)\sin\Omega_1 t\Big|\, dt, \quad (3.21)$$

where the averaging time τ can be a common multiple of the field oscillation periods $T_1 = 2\pi/\Omega_1$ and $T_2 = 2\pi/\Omega_2$. Numerical derivatives can then be used to obtain an expansion as in Eq. (3.8). This model is used to inform the design of the magnetic waveguide.

3.3 Trap design

Our interferometer apparatus uses a magnet design detailed by Horne *et al.* [43] The fields are produced by six coils mounted on the surface of a cube that is centered on the origin. Each individual coil consists of two planar spirals with seven turns each. The inner radius is 4.96 mm and outer radius is 10.24 mm. The spirals are located at distances of 10.56 mm and 11.32 mm from the cube center. A drawing of the cube trap and its mount is shown in Fig. 3.2. If we approximate the spirals as current loops at their average radii and distances, we obtain $\gamma = 2.01$ cm^{-2}, $\xi = 0.81$ cm^{-2}, and $\eta = 0.66$ cm^{-4}. In comparison, numerically calculating the field from the true spiral geometry gives an axial Taylor expansion about the origin of

$$B(z) = B_0\left(1 - 1.81z + 1.94z^2 - 1.48z^3 + 0.76z^4\right) \tag{3.22}$$

where B_0 is the field at $z = 0$ and z is in cm. From this we can read off the field coefficients $\gamma = 1.94$ cm^{-2} and $\eta = 0.76$ cm^{-4}, and we obtain $\xi = (-1.48\text{ cm}^{-3})/(-1.81\text{ cm}^{-1}) = 0.82$ cm^{-2}. These differ from the single-loop approximation by less than 15%.

Using the exact coefficients to calculate the TOP potential at a bias $B_0 = 1.85$ G yields an oscillation frequency $\omega_0 = 2\pi \times 9.46$ Hz and geometrical parameters

$$\lambda^2 = 1.19 \qquad a = 0.80\kappa \qquad b = 0.64\kappa$$

$$c = -0.077\kappa^2 \qquad f = 0.61\kappa^2 \qquad h = 0.43\kappa^2, \tag{3.23}$$

with $\kappa = B_1'/B_0$ and $B_1' = 2mg/\mu$ as above. In comparison, the ideal results of

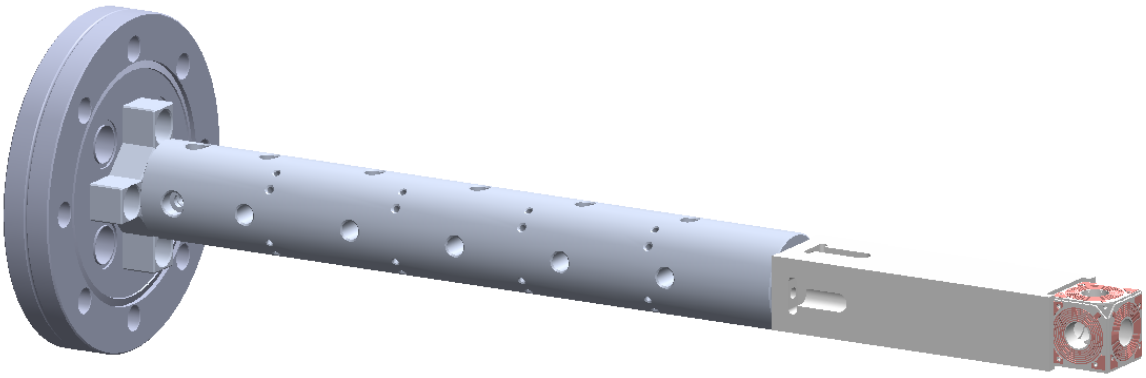

Figure 3.2: **A 3D drawing of the cube trap and its mount.** The waveguide is generated at the center of six coils mounted to a cube. The cube has 21 mm length sides, and ⌀10 mm aperture for optical access. The cube is mounted on a 100 mm long Boron Nitride structure, which is fixed to the vacuum feedthrough flange by a 25 cm aluminum arm [29, 33].

Eq. (3.10) give $\omega_0 = 2\pi \times 9.52$ Hz and

$$\lambda^2 = 1.14 \qquad a = 0.857\kappa \qquad b = 0.643\kappa$$

$$c = -0.0661\kappa^2 \qquad f = 0.607\kappa^2 \qquad h = 0.415\kappa^2. \tag{3.24}$$

The impact of the real coil geometry in this trap, including the spiral components, is only modest. If we increased the bias field to operate in a weaker trap, the impact of the geometry would be more significant.

3.4 Electronics

We now consider the current source electronics. Since the trap drive circuit was first built, we have made some small but significant changes to give the user easier control over the fields. For a comprehensive account of the original drive circuit, see [29]. Here, I will give a brief overview and explain the changes that were made.

See Fig. 3.3 for an up-to-date circuit diagram.

The original circuit used two function generators, one operating at f_1 = 1 kHz and the second at f_2 = 10 kHz. To make the quadrupole field, the 10 kHz field drove the z coils. To make the bias fields, the circuit mixes the two signals to drive the horizontal bias fields using a multiplier integrated circuit. A phase shift between the x and y bias coils is required, and that can be adjusted using a phase shifter op amp circuit. Analog input voltages control the amplitude of the bias and quadrupole fields, and these can be changed dynamically during the experiment. The signals are supplied to the coils through an audio amplifier, and a sense coil is used in a negative feedback loop such that the current supplied to the coils is stabilized with respect to variations in the amplifier gain and the load impedance [45].

The first change made to the drive circuit was to eliminate the analog phase shift component of the circuit, and add a third function generator. The three function generators are digitally phase locked. This change allows for easier control over the phase between the horizontal bias fields. It also improves stability introduced by that op amp, as phase locked oscillators are more stable than the phase shifter circuit.

A second change made is also related to the third function generator. With the original circuit, the amplitude of the bias fields are controlled with potentiometers. Any adjustment to the bias amplitudes must be made in between experimental runs, and requires measuring the signal on an oscilloscope. Now we are able to control the amplitude through the function generators' amplitude modulation. Using the analog input on the new function generator gives dynamic control over the current providing the x bias field. We also find this configuration to be more stable.

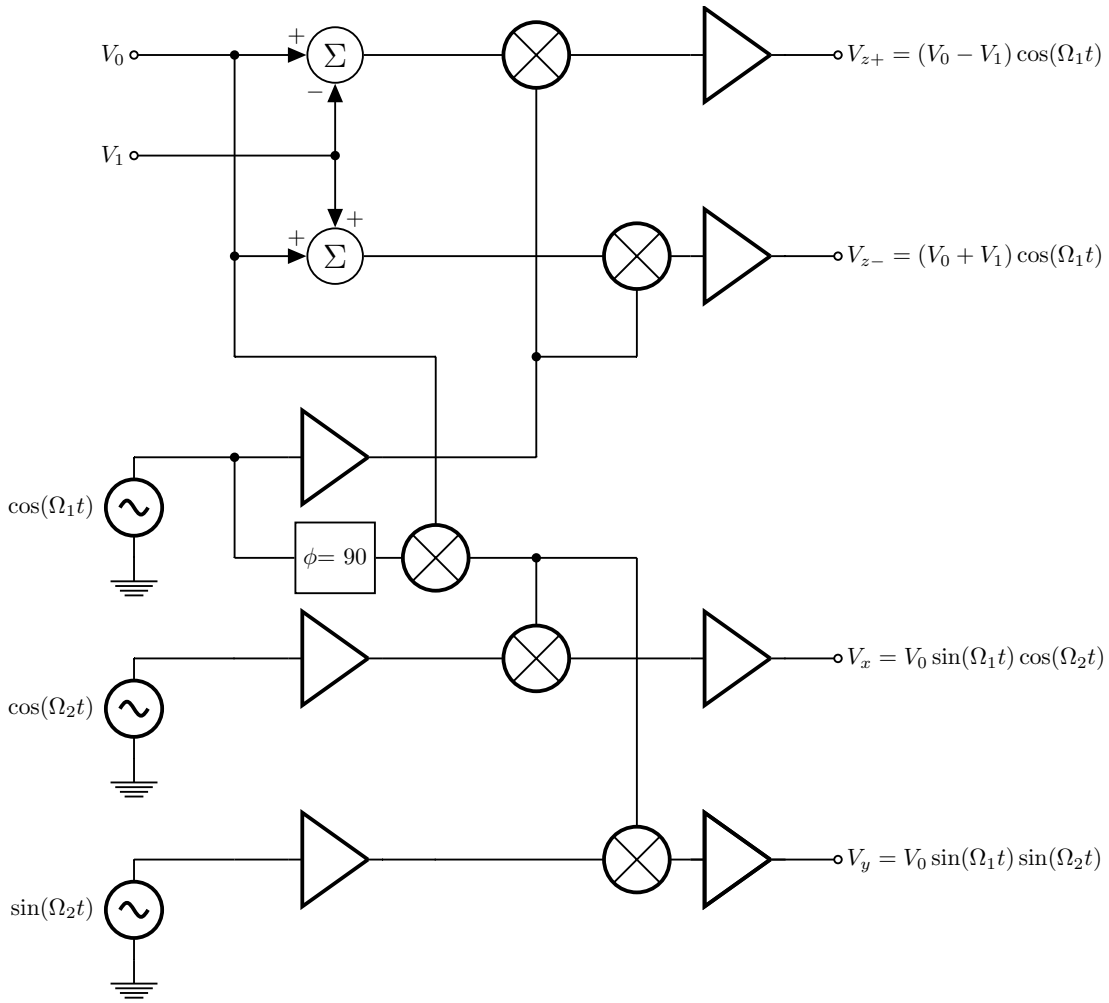

Figure 3.3: **A block diagram of the waveguide drive circuit.** The triangular elements are buffer amplifiers. The $\otimes$ elements are multipliers. Circles with Σ inside are summing amplifiers. Drive circuit inputs are on the left of the diagram, and outputs are on the right. This diagram does not include certain trap control parameters, like α and β. $V_{z\pm}$ are the signals for the top and bottom z coils, respectively. This figure reflects changes made to the circuit to include a third function generator. This figure was adapted from [29].

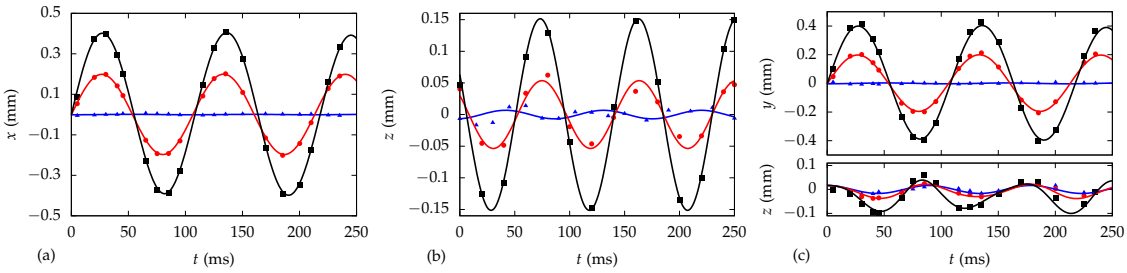

Figure 3.4: **Trajectories of atoms oscillating in the magnetic trap.** In (a) and (c), red and black data correspond to $2\hbar k$ and $4\hbar k$, respectively, and blue data are residual oscillations in the trap, tracked by the rest packet in the split. In (b), the trap is used to kick the condensate along z, with varying amplitude. In (c) the motion along both y and z are shown.

3.5 Oscillation measurements

We can experimentally characterize the trapping potential by using the atoms' oscillatory motion. This is the most direct method for characterizing the potential, and is a useful tool for reaching our goal of a Sagnac interferometer. Horizontal oscillatory motion can be induced with the Bragg beams. Recording the path of the atoms after a Bragg split is applied is relatively simple. Absorption images of the xy or yz plane are taken after allowing the atoms to oscillate for a range of propagation times. Momentum kicks of $2\hbar k$ and $4\hbar k$ can be applied, as shown in the data in Fig. 3.4.

We have no Bragg beam along $\hat{\mathbf{z}}$, so instead we induce motion along this direction with a magnetic kick. This is achieved by changing the quadrupole amplitude B_1' adiabatically, which vertically displaces the trap center and the condensate. The field is then rapidly switched back to its original amplitude, causing the condensate to oscillate along $\hat{\mathbf{z}}$. The size of the quadrupole field change controls the amplitude of the motion, as shown in Fig. 3.4(b).

For a one-dimensional oscillation, it is possible to develop an analytical perturbative series for the motion in terms of the anharmonic coefficients [46]. While motion in higher dimensions is more complicated, the trajectories considered here can be approximated as one-dimensional to the extent that the amplitude in one direction is much larger than the amplitude in the others. For instance, when we kick the atoms along y we see from Fig. 3.4(c) that the amplitude in y remains four times larger than that along z. When kicking along z, the excitation along x and y is smaller yet. The leading order effect of the anharmonicity scales as the amplitude squared, so we expect that treating the different motions as one-dimensional will lead to errors of less than 10%.

We seek to characterize the perturbation anharmonic terms introduced to the system, specifically how those terms might influence the horizontal oscillation frequencies. We start by deriving the equations of motion from the Langrangian for x,

$$\mathscr{L} = \frac{1}{2}m\dot{x}^2 - \frac{1}{2}m\omega_0^2 x^2 - \frac{1}{3}m\gamma x^3 - \frac{1}{4}m\eta x^4. \tag{3.25}$$

The equations of motion are of the form

$$\ddot{x} + \omega_0^2 x = -\gamma x^2 - \eta x^3. \tag{3.26}$$

Following Landau's development [47], we can find the effects of non-zero perturbations. For the horizontal motion, the only relevant anharmonicity is the quartic term $c\rho^4/4$. The perturbation analysis predicts this to cause the oscillation frequency to vary with amplitude A, as

$$\omega_\rho = \omega_0 + \frac{3c\,\omega_0}{8}A^2. \tag{3.27}$$

We do observe such a shift as seen in Fig. 3.5. From the slope and intercept of the

linear fit, we obtain $\omega_0 = 2\pi \times (9.5 \pm 0.2)$ Hz and $c = -0.31 \pm 0.03$ mm^{-2}. The uncertainty in c is comparable to the limits of the one-dimensional model.

Because the vertical motion is asymmetric, we expect both a cubic term $az^3/3$ and a quartic term $fz^4/4$. The cubic term will shift the center of oscillation by an amount

$$\Delta z = -\frac{a}{2\lambda^2} A^2, \tag{3.28}$$

where $\lambda = \omega_z/\omega_0$. We do observe such a shift, as seen in Fig. 3.5, although the effect is not large compared to the measurement accuracy. The fit shown gives a value for a/λ^2 of 1.0 ± 0.2 mm^{-1}, and the frequency measured at low amplitudes is $\omega_z = 2\pi \times (11.2 \pm 0.1)$ Hz. This gives $\lambda = 1.18 \pm 0.02$ and thus $a = 1.4 \pm 0.2$ mm^{-1}.

Both the cubic and quartic terms contribute to a shift in the oscillation frequency, as

$$\Delta\omega_z = \omega_z \left(\frac{3f}{8\lambda^2} - \frac{5\lambda^2 a^2}{12} \right) A^2. \tag{3.29}$$

We find $\Delta\omega_z$ to be consistent with zero, with a relative accuracy of 10^{-2} up to $A = 0.17$ mm. This indicates that the two contributions cancel so $f \approx (10/9)\lambda^4 a^2$. Based on the uncertainty in a, λ and $\Delta\omega_z$, we find $f = 4.5 \pm 1.5$ mm^{-2}.

We are not aware of an analytical method to determine the coefficients b and h, which couple the horizontal and vertical motions. To determine these values, we fit data such as in Fig. 3.4(c) to calculated trajectories in a model potential with the form of Eq. (3.8). We fix all parameters except b and h to the values determined above. The b and h parameters are then adjusted to provide the best fits to the data set. This yields $b = 1.0 \pm 0.3$ mm^{-1} and $h = 3 \pm 1$ mm^{-2}. The uncertainties are determined from the quality of the fit, as the variations needed to increase χ^2 by

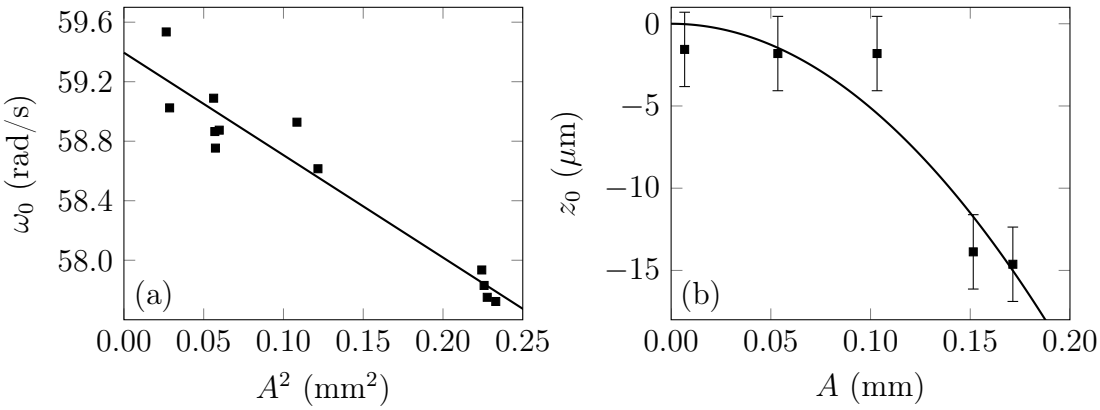

Figure 3.5: **Data showing the asymmetry along $\hat{\mathbf{z}}$.** The frequency decreases as A^2 as shown in (a), where a harmonic trap would remain constant. (b) shows the center of the oscillation depends on the size of the oscillation. Points are data fitted to the form of Eq. (3.28). Error bars are based off of sinusoidal fits.

about a factor of 1.5. These uncertainties are larger than the changes observed when the fixed parameters in the potential are varied by their own uncertainty. We also used this model to verify that the horizontal frequency shift depends only on c: if we allow c as a free parameter in the trajectory fit, we get a value consistent with the frequency-shift result but with a larger uncertainty.

Our results are summarized and compared to predictions in Table 3.1. While most of the observed values are consistent with the predictions, the values of λ and c differ by more than three standard deviations. The reason for this is not clear, but one possibility is that the bias field amplitude in the z direction differs from that along x and y. We have observed that this affects λ.

Ultimately, we hope to improve the accuracy with which the anharmonic coefficients can be measured. This might be achieved by driving motion with larger amplitudes, measuring the trajectories for longer times, and improving the stability of the trap fields. It may also be possible to find different trajectories that allow the

Parameter	Predicted value	Observed value
$\omega_0/2\pi$ (Hz)	9.46	9.5(2)
λ	1.09	1.18(2)
a (mm^{-1})	1.33	1.4(2)
b (mm^{-1})	1.06	1.0(3)
c (mm^{-2})	-0.21	-0.31(3)
f (mm^{-2})	1.68	4.5(1.5)
h (mm^{-2})	1.18	3(1)

Table 3.1: **Trap potential parameters as in Eq. (3.8).** Predicted values are from Eq. (3.24) with $\kappa = 1.66$. The corresponding bias field $B_0 = 1.85$ G was chosen to make the predicted and observed ω_0 values agree, and is consistent with the experimental calibration $B_0 = 2.0 \pm 0.1$ G.

coupling parameters like b and h to be more clearly distinguished.

3.6 Circular trajectories

In our Sagnac interferometer experiment, we send the atoms around the trap along a ring. Because this is a dual-Sagnac interferometer, we require two separate pairs of wave packets to propagate along a ring, starting at opposite sides of the trap. After completing one complete orbit, each pair of clouds needs to be well-overlapped to exhibit interference. Therefore before implementing interferometry, we worked to make the trajectories as circular as possible (instead of, say, elliptic), and also worked to ensure the trajectories remained as flat as possible along z.

Figure 3.6(a) illustrates the ideal procedure. First, the BEC, initially at rest at the origin, is split by applying the Bragg beam along y. This generates two wave packets with velocities $\mathbf{v} = \pm v_B \hat{\mathbf{y}}$. The wave packets move in the trap, with their centers of mass following the ordinary trajectory for a harmonic oscillator, $x(t) = 0$

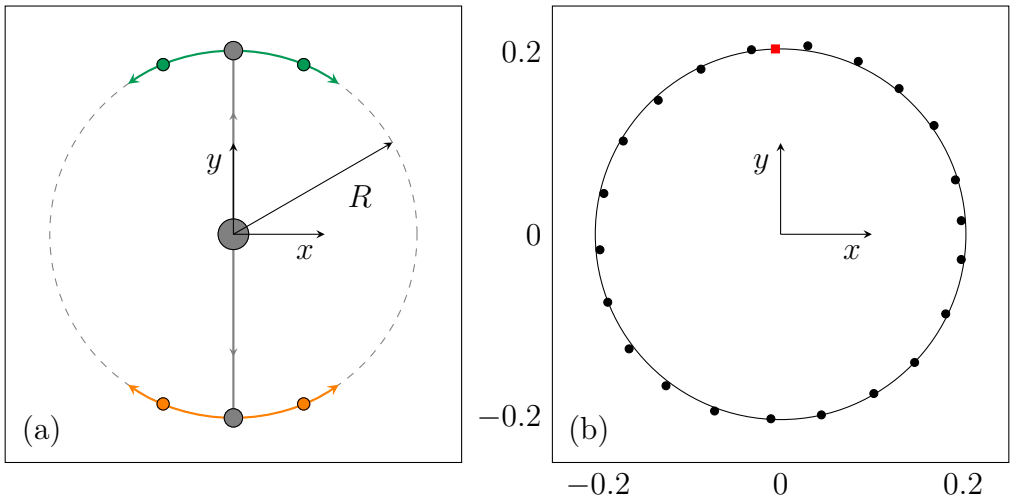

Figure 3.6: **Overview of circular trajectory procedure.** (a) A schematic of the circle splitting procedure. The initial condensate (center) is split into two packets that move along $\pm y$. When the packets reach their turning points at $y = \pm R$, they are split along x, generating four packets which move in circular orbits (green and orange traces). (b) Experimental data showing the path of one packet, starting at the red square and moving counterclockwise in 5 ms increments. The scales are in mm.

and $y(t) = \pm(v_B/\omega_0)\sin\omega_0 t$. After a time $t_1 = \pi/(2\omega_0)$, the atoms come to rest near the classical turning point at a radius $R = v_B/\omega_0$. The Bragg beam along x is then applied to both packets, providing velocity kicks $\pm v_B\,\hat{\mathbf{x}}$ and generating a total of four packets. Each of these packets now travels in a circle with radius R, as $x(t) = \pm R\sin\omega_0 t$ and $y(t) = \pm R\cos\omega_0 t$. In the interferometer, the atoms propagate for time $t_2 = 2\pi/\omega_0$, completing one full orbit around the trap. Here, however, we aim to study the circular trajectory of the clouds. Similarly to the 1D oscillation measurements, we image the system for different times t_2 in order to get a complete picture. A video summarizing the experiment can be found in the supplemental material of [53].

An example of one of these measurements is shown in Fig. 3.6(b). It is obviously not a perfectly circular trajectory as it strays from the circular best-fit line, but this was sufficient to see interference. Some of the key factors that determine the

path traversed by the atoms include the degeneracy of the x and y trap frequencies, the presence of certain anharmonicities, and the Bragg beams' incident angles on the atoms. With a thoughtful experimental setup, it is relatively simple to make adjustments to one of these parameters and measure its effect on the trajectory. In some cases, the effect is characterized not with the circular trajectory, but with 1D linear oscillations instead. The effects on the circular trajectory can be measured by fitting the path of one cloud to an ellipse, focusing on achieving a ratio of the major and minor axes equal to unity.

3.6.1 Bias field adjustments

The first step in achieving closed circular loops is ensuring the horizontal trap frequencies are equal, and that the phase between the horizontal bias fields is not introducing undesirable cross terms. Here, we assume the higher-order effects are small, and consider just the fundamental oscillation frequencies. The bias fields are

$$B_x(t) = B_0\Big[(1+\alpha)\sin(\Omega_1 t)\cos(\Omega_2 t+\beta)\Big], \tag{3.30}$$

and

$$B_y(t) = B_0\Big[(1-\alpha)\sin(\Omega_1 t)\sin(\Omega_2 t-\beta)\Big]. \tag{3.31}$$

The parameters α and β are controlled with the drive circuit's function generators. To adjust α, we adjust the ratio of the bias currents, I_x and I_y. These can be scaled together during the experiment by adjusting the amplitude of the parameter B_0, controlled through an analog voltage. This allows for simple rough adjustment of the trap tightness. The parameter α allows us to control the relative amplitude of

the horizontal bias fields by an independent amplitude modulation on the function generator controlling B_x. The phase parameter β is also adjusted with the function generators. We set the angle between the bias signals roughly equal to 90° so β is nominally zero, and can be adjusted to 1 mdeg. Assuming the Bragg beams are aligned with the principle axes of the trap, we can consider how these small parameters impact the potential,

$$U = U_0 - \frac{1}{2}\mu B_1 z + \frac{1}{2}m\omega_z^2 z^2 + \frac{1}{2}m\omega^2\left[\left(1+\frac{\alpha}{7}\right)x^2 + \left(1-\frac{\alpha}{7}\right)y^2 + \frac{2}{7}\beta xy\right]. \tag{3.32}$$

We can see from Eq. (3.32) that the amplitude adjustment α will impact the trap frequencies along x and y. To symmetrize the trap to first order, we first measure ω_y by taking trajectory measurements, like those shown in Fig. 3.4(c). We split along $\hat{\mathbf{y}}$ with $2\hbar k$ momentum kicks, since higher-order terms effect the larger momentum kicks. The trajectories are measured over the course of a few oscillation periods, and the data can be fit to a first-order sine wave. The same procedure is used to measure ω_x, which can then be adjusted to match ω_y with the bias amplitude adjustment, α. The frequency scales linearly with the amplitude of the signal.

The ratio of the bias current amplitudes, $I_x/I_y = 0.75$ to symmetrize the trap. The reason for the large discrepancy in the field amplitudes is not clear because the coil geometries are nominally the same, with similar electronic characteristics. Obviously, a more complete approach includes considerations beyond first-order terms, and is likely required in a more robust effort to make circular trajectories. Unfortunately, accessing these terms is not simple with the trap drive circuit.

We can also see from Eq. (3.32) that the phase between the horizontal bias fields, β, gives rise to a coupling between the two spatial axes. Effectively, this rotates

the principle axes of the potential away from the spatial axes, which on its own can break the overlap of the clouds when they pass each other. We found that setting the function generators with $|\beta| \leq 1^\circ$ was sufficient to maintain the overlap in the circular trajectories.

3.6.2 Bragg angle adjustments

The Bragg optics allow for precise adjustment of the pitch and yaw of the beams with respect to the trap. We define x y and z to be the lab coordinates. There are several things to consider about the angles of the Bragg beams, viz. the angles between the beams and the lab frame, and the angle between the Bragg beams themselves. The wave vector of each beam can be written in the lab frame coordinates,

$$\mathbf{k}_x = \cos\psi_x\,\hat{\mathbf{x}} + \sin\psi_x\cos\xi_x\,\hat{\mathbf{y}} + \sin\psi_x\sin\xi_x\,\hat{\mathbf{z}}, \tag{3.33}$$

and

$$\mathbf{k}_y = \sin\psi_y\cos\xi_y\,\hat{\mathbf{x}} + \cos\psi_y\,\hat{\mathbf{y}} + \sin\psi_y\sin\xi_y\,\hat{\mathbf{z}}. \tag{3.34}$$

We assume the Bragg beams are retro-reflected without error. Because of the curvature of the x Bragg beam wavefront, the atoms at $y = \pm R$ experience non-parallel momentum kicks, but this effect is small. Ideally, of course, $\mathbf{k}_x = \hat{\mathbf{x}}$ and $\mathbf{k}_y = \hat{\mathbf{y}}$. The $\hat{\mathbf{z}}$ component of the beams can be controlled with the tilt of the mirror in each Bragg beam path. We also need to ensure the Bragg beams are perpendicular to each other, which we can do by comparing the position of the clouds shortly after being split along $\hat{\mathbf{x}}$ and shortly after being split along $\hat{\mathbf{y}}$. The two clouds in each 1D split form a line, and we can measure the angle between those two lines.

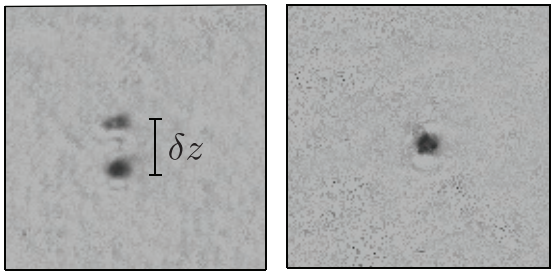

Figure 3.7: **Images of the yz plane after one orbital period.** The pitch of the y Bragg beam is adjusted such that the clouds are coincident. The size of one of the clouds is 15 μm. In the image on the left, the clouds pass over and other each other at one period. The right image shows the two clouds coincident at one period.

Following the procedure to split the condensate into four wave packets traveling in a circle, we observe the clouds using the side camera to determine whether the clouds pass through each other or whether they miss. This requires two conditions to be met. The first is that the pitch of the y Bragg beam is level enough as to not change the z value of the two clouds as they propagate to their turning points. The second condition is on the x Bragg beam. The pitch of the x Bragg beam determines the trajectories as the clouds propagate around a circle.

We require the atoms to be well-overlapped in phase space, i.e. to be physically coincident, with anti-parallel velocity vectors. The extent to which the clouds need to be overlapped is given by the Thomas-Fermi approximation [48], which gives the size of the clouds as

$$L = \sqrt{\frac{2\mu}{m\omega_0^2}} = 15\ \mu\text{m}, \tag{3.35}$$

where m is the mass of a rubidium atom, ω_0 is the horizontal trap frequency. The chemical potential $\mu = 2\pi\hbar \times 40$ Hz. Assuming an ideal potential, the atoms propagate over a distance of $4\pi R \approx 2.5$ mm before they should overlap. To maintain a reasonable $1/e$ overlap of the clouds, that limits the angular deviation of the Bragg beams to be less than $0.13°$. This is large compared to the angular resolution of the Bragg steering

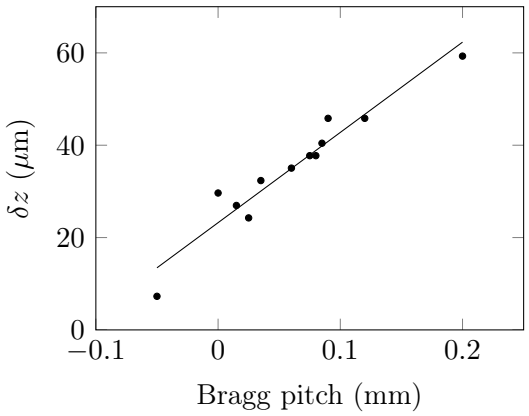

Figure 3.8: The distance between the two clouds, δz, after one orbit is measured as a function of the y Bragg beam's pitch. The horizontal axis is the tip-tilt mirror mount micrometer reading.

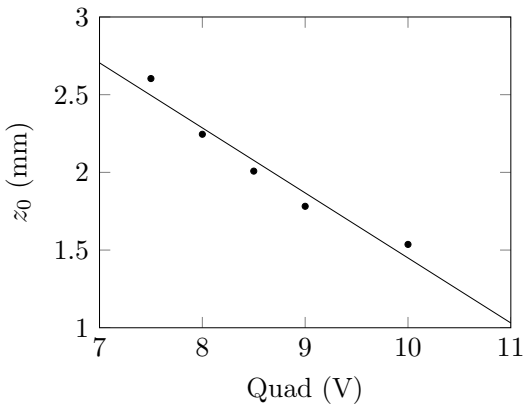

Figure 3.9: To ensure the pitch of the x Bragg beam can be adjusted fully, the height of the condensate needs to be adjusted with the quadrupole amplitude.

mirrors, which is about 0.02°, but this is also an upper limit to the allowable angular range.

Experimentally, it is simple to verify the overlap of the clouds. We ensured the overlap of the clouds by probing the atoms at exactly one period. We adjusted the x pitch until we saw the pairs of clouds coalesce. The sizes were consistent with an image taken before the atoms are split the second time along x. This also gives a good estimate for the interferometer time, t_2. Using the side camera, we are able to verify the clouds are overlapped along z. Using the same procedure of taking an image when the clouds pass by each other, we observe either two clouds passing over and under each other, or one cloud, like the absorption images shown in Fig. 3.7. Because the Bragg steering mirrors have micrometers, we are able to measure the vertical displacement of the clouds, δz, as a function of the Bragg's angular pitch. Those results are shown in Fig. 3.8.

A consideration when adjusting the pitch of the x Bragg beam is the optical access. We found that Bragg beam could be adjusted over a wide range while maintaining overlap between the clouds, but found that the waveguide cube structure would clip the beam. It was necessary to adjust the height of the cloud, z_0, to better center the cloud on the cube openings. We achieved this by adjusting the quadrupole field amplitude. Without a significant effect on the trajectories, we were able to relocate the cloud such that it was more central in the structure, giving us the largest range of optical access. The height's dependence on the quadrupole strength is shown in Fig. 3.9.

To summarize, we were able to make adjustments to the experiment to produce two pairs of clouds that propagate in a circle. The trapping potential must be adjusted such that the horizontal trapping frequencies are in agreement, which is achieved with amplitude modulation on the x bias field. Note that this procedure also gives rough estimates of the timings, t_1 and t_2. The Bragg beams must be adjusted such that the angles between the two beams is normal, and that their relative angles to the trap's principle axes are sufficiently small. We experimentally verify that the overlap is achieved at one period using both the side and top imaging systems. A comprehensive study of how these can influence the interferometer's performance will not be included here, but is well-summarized in a recent paper by West [49].

4 Interference measurements

The efforts discussed in the previous chapter were undertaken in order to make the trap suitable for atom interferometry measurements. In this chapter, some of those interferometry measurements will be discussed, including the first measurement of a physical rotation using confined atoms. With our setup used to create circular orbits, we produce two simultaneous interfering signals. The beauty of this approach is that common-mode noise, such as vibrations, can be canceled. By rejecting such sources of noise, we are able to use this system to measure small physical rotations. This is the culmination of a ten-year-long effort, beginning with the adaptation of our linear magnetic waveguide to a cylindrical trap. A few other measurements are included, which illuminate how the interferometer responds to experimental parameters other than a physical rotation.

4.1 Interferometer operation

As mentioned previously, we use the Bragg beams to create four wave packets traveling around the trap in a circle. A step-by-step of the experiment is included in Appendix A.2. To recap the procedure: first, the condensate is split along $\hat{\mathbf{y}}$. The two clouds

are allowed to oscillate freely for a time t_1, which is nominally when the clouds come to rest at one-quarter period. After that, they are split again, this time along $\hat{\mathbf{x}}$. They now have the requisite momentum kicks to travel in circles. The four clouds are allowed to propagate along their circular path for the *interferometer time*, t_2, which is nominally one full period. Before considering how the pair of interferometers work together to measure rotations, we consider just one measurement independently. Before the atoms are split along $\hat{\mathbf{x}}$, we consider them to be in the zero-momentum state, $|0\rangle$. The ideal splitting operation couples this state with the superposition of the two momentum states, $|\pm v_B\rangle$, with the indicated velocity along $\hat{\mathbf{x}}$. We can define a unitary operator that describes this process,

$$U_{\text{split}}|0\rangle = |\text{split}\rangle \equiv \frac{1}{\sqrt{2}}(|+v_B\rangle + |-v_B\rangle), \tag{4.1}$$

and the reverse operation also holds,

$$U_{\text{split}}|\text{split}\rangle = |0\rangle. \tag{4.2}$$

After propagating through the trap for one period, the pair of clouds is overlapped again. Their wave function can be expressed as

$$|\psi\rangle = \frac{1}{\sqrt{2}}\left(e^{i\Phi/2}|+v_B\rangle + e^{-i\Phi/2}|-v_B\rangle\right), \tag{4.3}$$

where Φ is the phase developed between the packets. After the recombination pulse is applied, the fraction of atoms returned to rest depends on Φ. The even superposition $(|+v_B\rangle + |-v_B\rangle)$ is coupled back to the zero-momentum state $|0\rangle$, as defined in Eq. (4.2), while the odd superposition $(|+v_B\rangle - |-v_B\rangle)$ remains unchanged (up to an overall phase). Projecting the wave function $|\psi\rangle$ onto this basis, we find that a fraction of the atoms

are brought back to rest [50, 51],

$$\begin{aligned}\frac{N_0}{N} \equiv S &= |\langle \text{split}|\psi\rangle|^2 \\ &= \frac{1}{4}|1 + e^{i\Phi}|^2 \\ &= \cos^2\left(\frac{\Phi}{2}\right).\end{aligned} \tag{4.4}$$

Using a trigonometric identity, the output signal S can be expressed as

$$S = \frac{1}{2}(1 + \cos\Phi). \tag{4.5}$$

The atoms that return to $|0\rangle$ now oscillate along $\hat{\mathbf{y}}$. The remaining atoms stay in $|\pm v_B\rangle$, so they continue along their circular path. We wait 12 ms for these clouds to separate, and then we turn off the trap and image the system with the top camera. A typical absorption image is shown in Fig. 4.1(a). Each of the six clouds is fit to a 2D Gaussian to determine their populations, such that S can be determined. Because there are two interfering pairs, we define $S_\pm$ to be the signal at $y = \pm R$, respectively.

The phase that develops between the two clouds has several different sources. Some phase contributions can be classified as noise. Because the atoms are held in a trap, noise can come from the trapping fields themselves or from mechanical vibrations, which cause a small shift between the Bragg split and recombination pulses. Because such sources of noise are present, we expect an interferometer signal S to also be noisy. In fact, we use this noise as an indicator that the interferometer is working.

When two clouds are not well-overlapped, the applied Bragg beams actually split

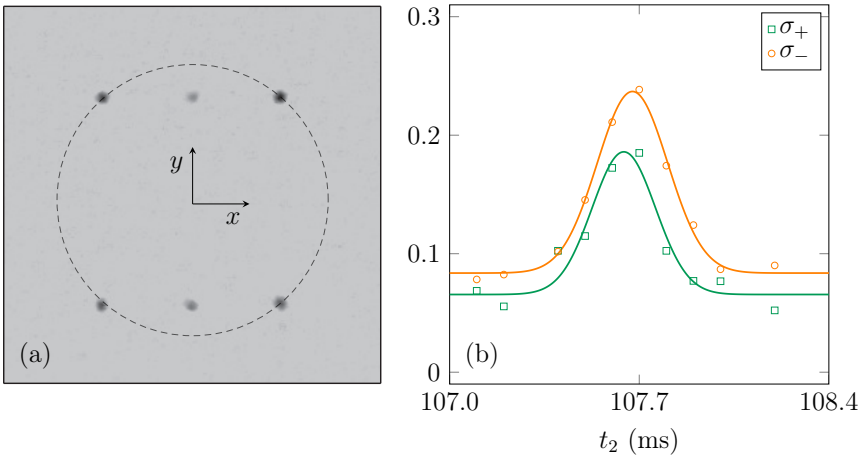

Figure 4.1: **An illustration of interference.** (a) An absorption image in the xy-plane taken 12 ms after the recombination pulse was applied. Atoms that were brought back to rest now oscillate along $\hat{\mathbf{y}}$, while the remaining atoms continue to move along the dashed circle. Here, the fraction of atoms brought to rest is small in both interferometers, indicating that both interferometers measure a phase close to π. (b) The standard deviations of the interferometer output signals, $\sigma_\pm$, are plotted as the interferometer time t_2 is varied. The waists of the Gaussian fits agree with the expected interaction time predicted by the Thomas-Fermi approximation.

each cloud again instead of recombining them. We can rewrite the two momentum states as a superposition of the symmetric and antisymmetric wave functions,

$$|+v_B\rangle = \frac{1}{2}\Big((|+v_B\rangle + |-v_B\rangle) + (|+v_B\rangle - |-v_B\rangle)\Big) \tag{4.6}$$

and

$$|-v_B\rangle = \frac{1}{2}\Big((|+v_B\rangle + |-v_B\rangle) - (|+v_B\rangle - |-v_B\rangle)\Big). \tag{4.7}$$

Since U_{split} couples the symmetric state back to the rest state $|0\rangle$, and has no effect on the antisymmetric state,

$$U_{\text{split}}|+v_B\rangle = \frac{1}{2}\Big(|0\rangle + (|+v_B\rangle - |-v_B\rangle)\Big), \tag{4.8}$$

$$U_{\text{split}}|-v_B\rangle = \frac{1}{2}\Big(|0\rangle - (|+v_B\rangle - |-v_B\rangle)\Big). \tag{4.9}$$

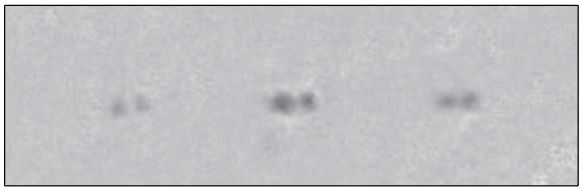

Figure 4.2: **An image showing poor recombination.** Instead of interfering with each other, the applied Bragg pulse splits the two traveling wave packets again, creating a total of six clouds in each of the interferometers.

So projected back onto the three-state basis, we find that after applying the recombination pulse the population in $|0\rangle$ is $1/2$, and each of the momentum states is $1/4$. This happens to both clouds, so there are six total clouds per interferometer. These nominally track together, so we see the outputs $S_\pm \approx 0.50$, with $\sigma_\pm \lesssim 0.05$, which is non-zero because of imaging noise. Given enough time to separate, the six clouds are clearly visible, which is shown in Fig. 4.2.

To characterize the performance of interference, we measure the signal several times for both interferometers. We calculate the standard deviation of the output signals, $\sigma_\pm$, between each set of data. This is simply the spread in S. The performance of interferometers is often measured by visibility V, which is mathematically related to the standard deviation:

$$\begin{aligned}\sigma^2 = \Delta S^2 &= \langle (S - \bar{S})^2 \rangle_\Phi \\ &= \langle (V/2 \cos\Phi)^2 \rangle_\Phi \\ &= \frac{V^2}{8}.\end{aligned} \tag{4.10}$$

We typically see peak visibilities around 0.5; in this thesis we report the interferometer performance in terms of the standard deviation. When a pair of clouds is well-overlapped, we see the random noise sources begin to write noise onto the in-

terferometer signals, seen as a spike in $\sigma_{\pm}$. This is illustrated in Fig. 4.1(b). The interferometer time t_2 was adjusted and the standard deviation was measured for ten data. The two interferometers exhibit optimal interference around $t_2 = 107.7$ ms.

Referring back to Eq. (3.35), we reconsider the issue of overlap in the context of the interferometer. The clouds are all approximately 15 μm wide. With the speed of the condensates, $v_B = 12$ mm/s, defined by the Bragg split, they should maintain an overlap of one cloud width for 230 μs, which agrees with the measured interaction time in Fig. 4.1(b) of 260 μs and 234 μs for the top and bottom interferometers, respectively.

4.2 Dual Sagnac interferometer

The sequence described above produces two independent interferometer measurements. Following the same naming convention, we define Φ_+ as the Sagnac phase measured for atoms at $y = +R$, and Φ_- as the phase measured at $y = -R$. In this implementation, with two simultaneous counter-propagating interferometers, the sources of random phase noise are common to both measurements. While one interferometer operating alone appears to have a random output, the pair of interferometers work in concert to reveal other sources of phase. The interferometers experience the same noise, making sources of differential phase stable, such as rotation. To see how, consider the system rotating with angular velocity $\mathbf{\Omega}$. The Sagnac phases,

$$\Phi_{\pm} = \pm\frac{1}{\hbar}\oint \Delta\mathbf{L}\cdot\mathbf{\Omega}\,dt = \pm\frac{4m\Omega A}{\hbar}, \tag{4.11}$$

will have the opposite sign. Here $\Delta\mathbf{L} = \mathbf{r}_2 \times \mathbf{p}_2 - \mathbf{r}_1 \times \mathbf{p}_1$ is the difference in angular momentum between the two packets, and $A = \pi R^2$ is the area of a single packet's orbit. The sign of the phase depends on whether $\Delta\mathbf{L}$ has the same or opposite sign as $\mathbf{\Omega}$. The rotation is then revealed in the differential phase,

$$\Delta\Phi = \Phi_+ - \Phi_- = \pm\frac{8m\Omega A}{\hbar}. \tag{4.12}$$

Now we consider how to extract the differential phase. Returning to the output signal in Eq. (4.5), we can be more specific about the argument of the cosine by separating the random phase from sources that are not common-mode. We can rewrite that expression as

$$S_\pm = C_\pm + A_\pm \sin\left(\Phi_N \pm \frac{\Delta\Phi}{2}\right), \tag{4.13}$$

where $C_\pm$ are the centers of the output signals, and $A_\pm$ are the amplitudes of the oscillations, roughly related to the visibility. Here, Φ_N incorporates all forms of common-mode phase noise, and will fluctuate from shot to shot. We can define

$$X = \frac{S_+ - C_+}{A_+} = \sin(\Phi_N + \Delta\Phi/2) \tag{4.14}$$

and

$$Y = \frac{S_- - C_-}{A_-} = \sin(\Phi_N - \Delta\Phi/2) \tag{4.15}$$

These terms can be combined in a specific way,

$$\frac{1}{2}(X^2 + Y^2) = \sin^2(\Phi_N)\cos^2(\Delta\Phi/2) + \cos^2(\Phi_N)\sin^2(\Delta\Phi/2), \tag{4.16}$$

and

$$XY = \sin^2(\Phi_N)\cos^2(\Delta\Phi/2) - \cos^2(\Phi_N)\sin^2(\Delta\Phi/2). \tag{4.17}$$

The common phase Φ_N can be eliminated using $\sin^2\Phi_N + \cos^2\Phi_N = 1$, and the equations can be combined to make the characteristic equation for an ellipse [28],

$$X^2 + Y^2 - 2XY\cos(\Delta\Phi) = \sin^2(\Delta\Phi). \tag{4.18}$$

Therefore we expect to see an ellipse in a plot of S_- against S_+, such as the simulated data in Fig. 4.3. The ellipse is centered at (C_+, C_-), with semi-major and semi-minor axes A_+ and A_-, respectively. So in order to extract the differential phase from our data, we fit the plot of S_- vs. S_+ to an ellipse in order to find $\Delta\Phi$.

We can also look at this through the lens of limiting cases for more clarity, referring back to Eq. (4.13). For simplicity, assume the centers of the signals are both 0.50, as we expect the signals to have a mean nominally equal to one half. We can also assume the signals have the same amplitude of 0.50, which is true for an interferometer with perfect visibility. For all limiting cases, we assume Φ_L is random, as we observe in the experiment. If the differential phase $\Delta\Phi = 0$, then the two interferometers will have correlated outputs, i.e. the data will lie along a line with $S_+ = S_-$. In the case where $\Delta\Phi = \pi$, we observe anti-correlated outputs. In this case, the data also lie along a line, $S_+ = 1 - S_-$. The last limiting case is for $\Delta\Phi = \pi/2$, where the signals can be written down as sine and cosine of the same argument. In this case, the data lie along a circle. For a differential phase not equal to 0, $\pi/2$, or π, the data lie along an ellipse. In all cases, Φ_N distribute the data randomly around the ellipse, while the shape and orientation of the ellipse is defined by the differential phase between the two interferometers. The sensitivity of the interferometer is higher near $\frac{\pi}{2}$ than

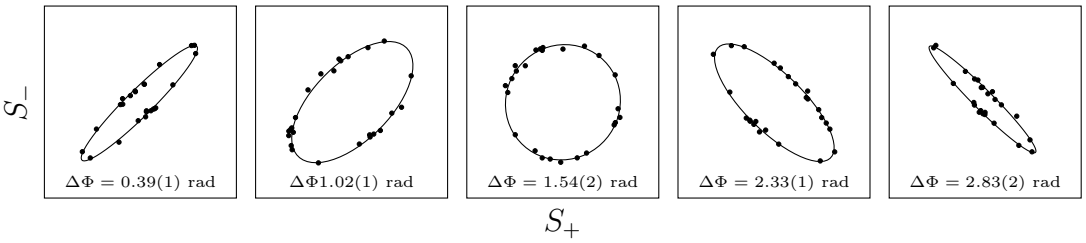

Figure 4.3: **Simulated data are fitted to a rotated ellipse.** The differential phases are increasing from left to right. All plots range from 0 to 1 on both axes. When $\Delta\Phi = 0$ or π, the data lie randomly along a line. When $\Delta\Phi = \pi/2$, the data lie along a circle.

it is near 0 and π. Using simulated data with similar noise to what we see in the experiment suggests the interferometer is five times more sensitive for a phase of $\frac{\pi}{2}$ than for one close to zero.

4.3 Trap sensitivities

Before covering the rotation measurements, it is important to consider some of the other sources of differential phase. As with the trap symmetry, there are several parameters that play a role here. While much of the computational analysis of these effects was not completed for this thesis, it was studied in parallel with the experimental research by my lab partner, Zhe Luo [52], whose thesis should be consulted for a more comprehensive picture. Even so, it is important to include these experimental findings, and characterize the influence of things like the Bragg beam angles, and the trapping field phases. In particular, we examined how these can influence the measured phase, $\Delta\Phi$, as well as the interferometer's contrast. For the latter, it is certainly important to document what sort of dynamic range the interferometer has, since diminished contrast results in lower phase sensitivity and inferior interferometer

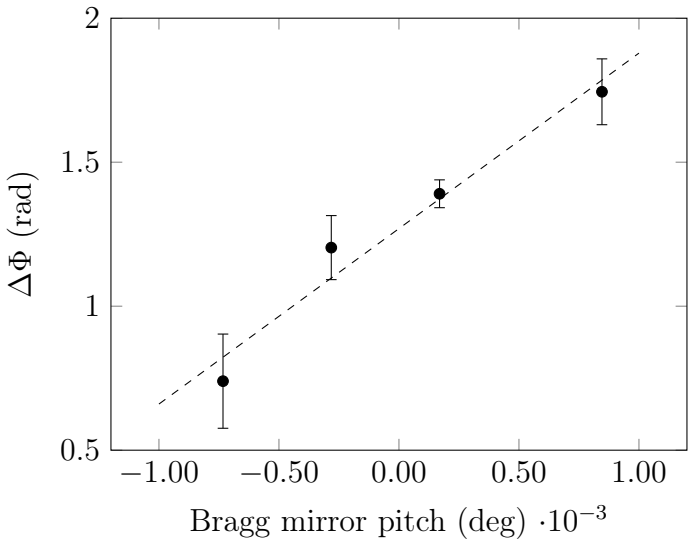

Figure 4.4: **The differential phase, $\Delta\Phi$, is measured as the pitch of the x Bragg mirror is adjusted.** Error bars are from the best-fit of the phase ellipse.

performance. But it is also important to understand how the differential phase can be adjusted, either to be zeroed out or to ensure the interferometer operates with an output near $\pi/2$.

4.3.1 Bragg beam angles

The Bragg beam optics were designed to give the user very fine control over their position and angle. Of course, the first concern is that the Bragg beams are aligned such that the clouds overlap after one orbit. That is, as described in the previous chapter, done by measuring their overlap on the top and side cameras. In an ideal trap, the Bragg beams should be able to operate in a range as large as 0.13°; outside that range the clouds will fail to overlap well enough to interfere. This is an upper limit, but is consistent with large operational range of the x Bragg beam.

The angle of the Bragg beams changes how the clouds traverse through the trap.

The differential phase's dependence on the x Bragg angle is shown in Fig. 4.4, which reveals a linear dependence, as we expect. The angular dependence is

$$\frac{d}{d\theta_{x\text{pitch}}}(\Delta\Phi) = 3.49 \times 10^{-4}. \tag{4.19}$$

We were not able to produce a similar measurement for the dependence on the y Bragg beam. The two Bragg beams behaved very differently. The x Bragg beam was forgiving, and could be adjusted over a wide range of angles and still exhibit interference. In fact, a plot of the contrast as a function of the Bragg pitch is not included here because the Bragg beam's optical access was obscured before the interferometer's contrast became sufficiently diminished. The opposite is true with the y Bragg beam. We were unable to measure any interfering signal after a small adjustment was made to the beam's angle, and was not easily recoverable. We believe the reason is related to the geometry of the beam path, as opposed to the behavior of the atoms in the trap.

4.3.2 Bias field adjustments, revisited

Another consideration is the trapping fields themselves, which influence the paths traversed by the clouds. We refer back to Section 3.6.1, specifically Eqs. (3.30) and (3.31). As a reminder, the parameter α controls the relative amplitude of the bias fields, and is set such that the horizontal trap frequencies are in agreement to first-order. The small parameter β is the phase angle between the horizontal bias fields, and gives rise to an xy cross-term in the potential. Those parameters are set such that the circular trajectories are closed loops, but we can also adjust them more finely to introduce an offset to the phase.

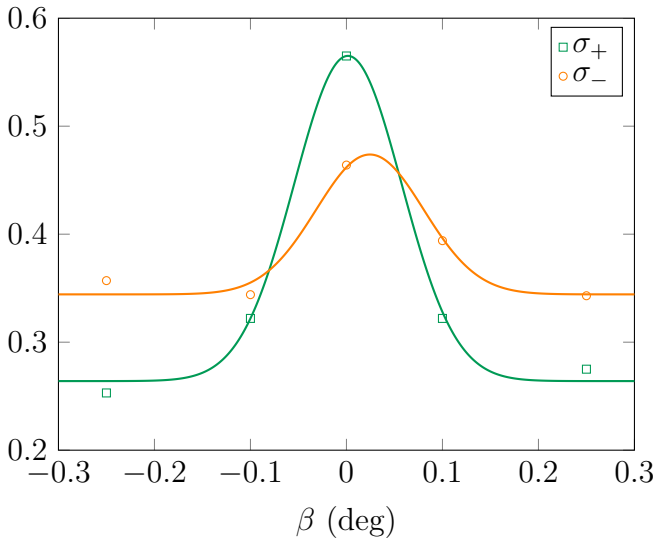

Figure 4.5: **The interference contrast is optimized in the bias phase, β.** Each datum here is the standard deviation over ten measurements with the same bias phase. Colors correspond to the cartoon in Fig. 4.1.

The first consideration is the interferometer's contrast as a function of the bias phase. By simply adjusting the β, we can see the operational range of the bias phase, which is shown in Fig. 4.5. Those data are taken without adjusting any other experimental parameter, and shows an operational range around 0.1°. As β is adjusted, the additional cross-term in the potential causes the wave packet trajectories to lose their overlap in position and velocity, which diminishes the contrast when the clouds are recombined.

The interference peak can be restored by adjusting other experimental parameters. One example we studied was adjusting the interferometer time, t_2. The results are summarized in Fig. 4.6. If β is changed, the interferometer contrast can be restored with compensating changes in t_2. We observed that complementary adjustments of β and t_2 were able to restore interference over a range of 1.0° in β, with a range of 0.5 ms in t_2. That is shown in the main plot of Fig. 4.6. We also measured how

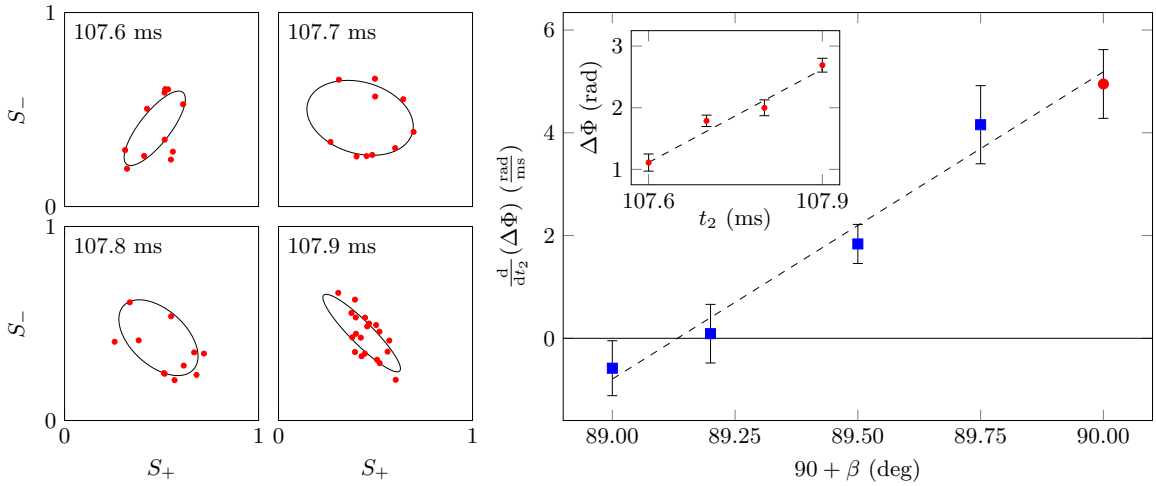

Figure 4.6: **For different bias phase shifts, $\Delta\Phi$ is measured as a function of t_2.** The red datum in the main plot corresponds to the inset, which is the compiled results from the raw data shown on the left.

the phase changes as a function of adjustments to β and t_2. For a given value of β, we measured $\Delta\Phi$ at several different interferometer times, as shown in the inset of Fig. 4.6, which shows a linear dependence on t_2. The slope of that line is dependent on the bias phase, and we were able to measure a zero-crossing in that time derivative. From the main plot, we find the dependence to be

$$\frac{d^2}{d\beta\, dt_2}(\Delta\Phi) = 6.0(5)\ \frac{\text{rad}}{\text{deg ms}}. \tag{4.20}$$

This measurement will be useful in a comparison with theoretical models of the phase evolution. Since we were able to measure a zero-crossing in the time derivative of the phase, we have shown that β can be set such that the phase has little or no time dependence, which makes this technique more suitable for sensor applications.

These derivatives are calculable, but that they appear to depend also on details of the trap anharomonicity. These will be a topic of future study. We will need to understand and have good control over these parameters in order to isolate the

Sagnac phase; however, as long as the additional differential phase is stable, it can be subtracted out for a rotation measurement.

4.4 Rotation measurements

Lastly, we return to the big picture of inertial navigation. The work described so far are steps towards the larger goal of building a rotation sensor. To reiterate a point made in Chapter 1, we are optimistic that matter-wave interferometers can outperform their optical gyroscope counterparts. To that end, we attempted to test the interferometer's performance at measuring rotations. However, this experiment sits on a large optics table and was not designed on a rotation stage, nor did we anticipate any need to miniaturize the apparatus for environmental testing. Therefore our efforts to test the sensor in a rotating frame gave rise to several engineering challenges. Since we have yet to fully characterize sources of differential phase other than rotation, we can measure only changes in the rotation rate instead of absolute rotations.

During the interferometry measurement, the experiment needs to be rotated with a constant and repeatable angular speed that can be adjusted between measurements. Because we have no built-in rotational system, we improvised a simple addition using a linear actuator. We chose to rotate the system by floating the optical table on air legs and pushing on a magnetic base fixed underneath it with the actuator (PI M-228), as shown in Fig. 4.7. The actuator has a travel distance of a few millimeters, and can travel at speeds up to 1 mm/s. With the table floating, the static required force to displace the table 3 mm was measured with a force gauge to be 10 N. The

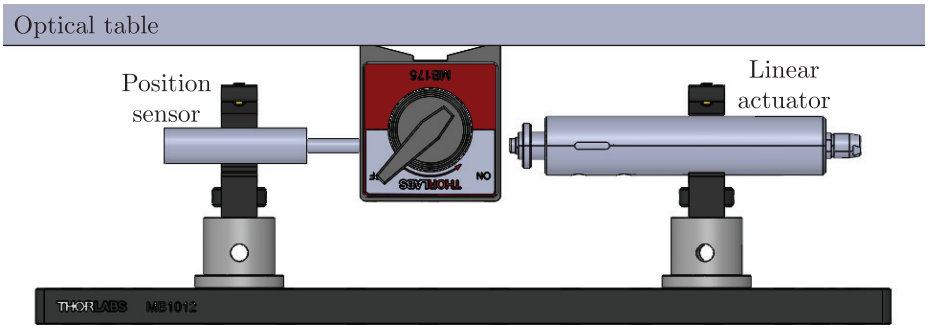

Figure 4.7: **The experiment is rotated using a linear actuator fixed underneath the table.** The linear actuator pushes on a magnetic base, fixed upside down to the optical table. A position sensor is mounted opposite the linear actuator to confirm that the translation speed and confirm the linear displacement during the interferometer measurement. The position sensor and linear actuator are mounted on the small breadboard shown here, which is fixed to a cross brace between a pair of the optical table's legs with C-clamps.

table can be allowed to rotate freely, or a fixed point can be introduced with a second magnetic base near a different leg.

For each interferometer measurement, the actuator is activated prior to the initial Bragg split along $\hat{\mathbf{y}}$, and continues at a constant speed v until after the clouds are recombined and imaged. Before the next experiment is run, the actuator retracts to its initial position. To confirm the motion is linear throughout the measurement, a position sensor is fixed opposite the actuator, and is monitored on an oscilloscope. This is also used to confirm the speed calibration of the actuator. We are also able to measure negative velocities by running the actuator in the other direction. The experimental sequence is summarized by the timing diagram in Fig. 4.8.

For a given speed of the linear actuator v, no fewer than ten measurements are taken, which are then fit to an ellipse, as described earlier in this chapter. The results of this experiment are shown in Fig. 4.9, which shows a clear sensitivity to rotation. The slope of the trend line is $\Omega/v = 162(15)$ rad/mm/s.

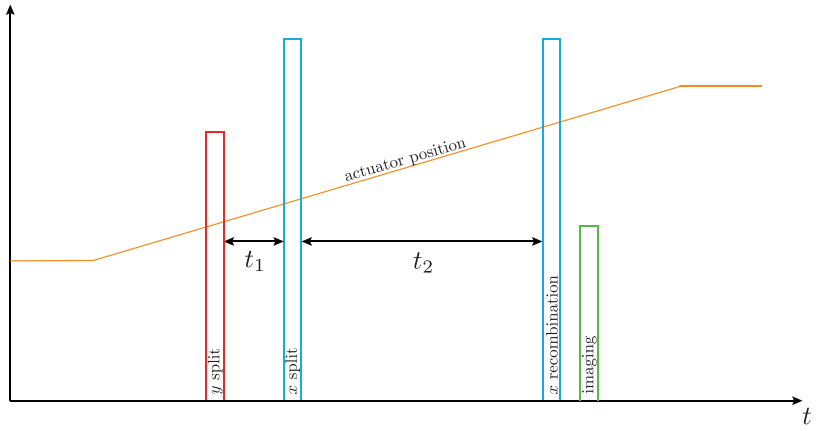

Figure 4.8: **A timing diagram summarizing the rotation experiment's sequence.** The orange line is position of the linear actuator, which can be monitored with the position sensor. The rectangular pulses represent the Bragg splitting pulses and the imaging step. The figure is not to scale.

Because the rotation measurements were not made using a dedicated rate table, accurate calibration of the rotation rate is difficult. Applying the Sagnac formula to the data in Fig. 4.9 indicates a rotation calibration v/Ω of 0.5 m. Initial tests using a dial gauge suggested the table rotated about a point 1 m from the translation stage, which is a larger discrepancy than expected.

In an effort to measure the table rotation more accurately, a HeNe laser was fixed to the optical table and split three ways so it was incident on four four-quadrant photodiodes, mounted in the lab along the coordinate axes of the table. The table was rotated in the same way it is during the experiment. This confirmed the rotation point was about 1.0(1) m from the translation stage, as we measured using a dial gauge. We also determined the table did not remain level during the rotation. By changing the weight distribution on the optical table, we were able to verify that the interferometer phase is insensitive to static tilts, and numerical calculations indicate no significant sensitivity to dynamic tilting at the level observed. The discrepancy between the mechanical measurement and the Sagnac formula will require further

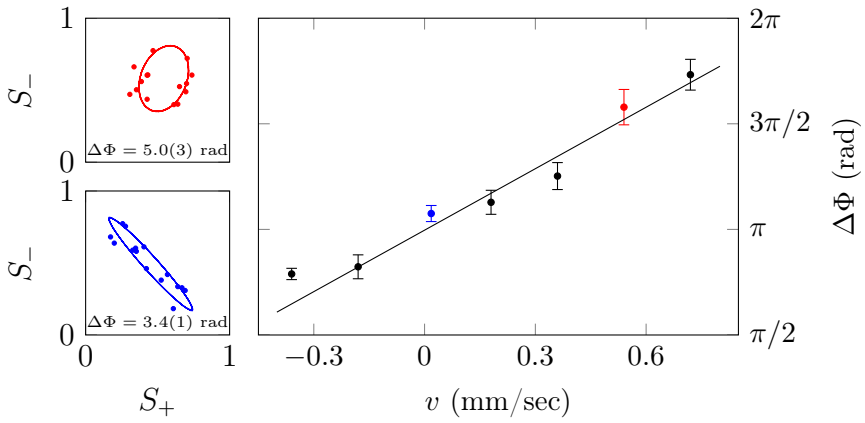

Figure 4.9: **Results from the rotation sensor experiment.** Left: Points correspond to the two interferometer output signals S_+ and S_- from a given measurement. Curves are ellipses fitted to the points. The orientation and eccentricity of the ellipse reveals the differential phase $\Delta\Phi$ between the interferometers. Right: Dependence of the differential phase on the experimental rotation velocity of the system v, illustrating the Sagnac effect. The offset at v = 0 mm/s indicates the trap is not perfectly symmetric. The shaded points correspond to the matching data on the left.

investigation.

The one-sigma error bars in the plot correspond to a rotation sensitivity of 8×10^{-5} rad/s, comparable to the rotation rate of the Earth, $\Omega_E = 7.3 \times 10^{-5}$ rad/s [53]. This rotation sensitivity is not exceptional, being about what a careful observer might obtain by watching the shadow of a sundial. An attractive sensitivity for inertial navigation applications is 10^{-7} (rad/s)/$\sqrt{\text{Hz}}$, corresponding to an angle random walk of 3×10^{-4} deg/$\sqrt{\text{hr}}$ [54]. Possible improvements to this technique are discussed in Sec. 5.1.

In summary, we have implemented a trapped-atom Sagnac sensor with the largest enclosed area to date, which for the first time uses simultaneous counter-rotating interferometers for common-mode noise rejection and demonstrates actual rotation sensing. The rotation sensitivity is comparable to Earth's rate, and we expect that

substantial improvements are feasible. We also note that our interferometer scheme could be of interest for fundamental physics. For example, it could be used to investigate the phase evolution of the trapped atoms themselves, which can exhibit nontrivial behavior such as phase diffusion [55] and squeezing [23].

5 ∴ Future work

The main goal of this work was to implement a trapped-atom dual Sagnac interferometer. After the design and construction of the magnetic waveguide, several years of work were spent devising methods for characterizing the trapping potential. Several improvements were made to make the trap more tunable. This dissertation summarizes the final experimental realization of the main goal. This is significant achievement, but is only a preliminary result. There are several areas of improvement we would like to explore, which are discussed in the next section. The lab will also continue work with an upgraded apparatus, as part of the DARPA A-Phi program. That new apparatus seeks to build a smaller and semi-portable rotation sensor based on the same principles of atom interferometry. Since this is the first experimental realization of a trapped-atom rotation sensor, there are several changes we believe would improve the experiment. Some of these changes are simple to implement with only minor changes, while other limitations are inherent to the experiment's geometry and timing limitations. We hope to rectify these more significant issues in the experimental design for our work in the APhi program.

5.1 Improvements to the rotation sensor

With the goal of the implementing an interferometer in this magnetic waveguide achieved, work should continue to build on this result by improving the rotational sensitivity of system. There are two simple ways to increase rotational sensitivity, $\frac{d}{d\Omega}(\Delta\Phi)$, both of which effectively increase the enclosed area. One way to double the sensitivity is to double the interferometer time and allowing the clouds to propagate twice around the trap. This will increase the precision required on the trap and Bragg beam alignment, but should be within reach. One might worry about the atom-atom interactions when the clouds pass through each other, which can reduce the interferometer contrast and also cause atom losses. In the weak trap, however, the density is low, around 10^{-4} cm^{-1}, so interactions are negligible.

We are also able to increase the sensitivity by changing the trap frequency. The trap frequency used in this work was about 10 Hz, but can be as low as 1 Hz. With a lower trap frequency, the Bragg kicks push the atoms further out in the trap. The sensitivity scales with R^2, so reducing the trap frequency can increase the trap sensitivity by orders of magnitude.

We chose to work with a 10 Hz trap mainly because of limits on Bragg laser power. In the circle split operation, the x Bragg beam splits the two clouds into four to induce circular motion. Because the two clouds are far apart, the laser is positioned such that the intensity is highest at the origin, with the two clouds located near the edges of the beam. That becomes trickier when the atoms are moved even further apart, as the beam profile needs to be made wider. One solution would be to use an astigmatic beam, with the profile focused down along $\hat{\mathbf{z}}$. The laser can also be tuned

closer to resonance, but that reduces the splitting operation's stability. It is expected that with the new Bragg laser we will have more power available, so this should not be an issue if the trapping frequency are reduced to 1 Hz.

Another area of improvement is the operational duty cycle of this experiment. With such weak magnetic traps, the adiabatic ramp from the initial dc TOP trap to the waveguide takes a considerable amount of time, about 12 seconds. In principle, this time can be optimized to achieve the same trap load without significant residual oscillations in about half that time. When the MOT loading and evaporation time is added on, the duty cycle is at least 40 seconds. Unfortunately, we determined the time limitations on the experiment are actually longer because of trap heating.

As determined by Horne [29] and investigated by Arpornthip [30], the waveguide heats up over time, and we saw this impact the trap frequencies. This effect is small over the course of one oscillation period; after the trap is kept running for 20 seconds the oscillation frequencies ω_x and ω_y changed by 2%. Because of this, the trap frequencies can become unstable, making it impossible to get the interferometer time t_2 correct, which we need to be within 0.1% of the true period. While we did not use such long hold times in the current experiments, we did observed the interference signal to degrade over the course of multiple runs. The effect is easy to see using the interferometer contrast. If the experiment is run with a short MOT loading time of 10 seconds, the contrast will be reduced to small and unmeasurable after 20 experimental runs. To fix this, we increased the MOT loading time to 60 seconds to allow the trap time to cool down.

It is worth noting that we expected the long-term thermal effects to be an order of magnitude smaller than this based on the thermal characterization when the trap

was constructed. We believe the most likely candidate for the discrepancy is the waveguide support structure becoming loose as the trap heats up. This might be avoided by attaching the coil chips to the cube in a different way, such as using vacuum-compatible epoxy. It is also possible this is related to thermal instability in the current sources themselves, or a change in copper resistance changes the current.

Finally, we can consider ways to reduce the effects of anharmonic terms in the potential. One promising approach is the addition of harmonic terms in the bias drive signals. Adding the third harmonic, $3\Omega_2$, to the field gradient allows for dynamic control over the condensate oscillations. We are also considering adjustments to the coil geometry, and altering the confinement strength during t_1.

5.2 A-Phi program

Work will continue with a new project called Bragg Interferometer Gyroscope in a Time-Orbiting Potential (BIGTOP) in DARPA's Atomic-Photonic Integration (A-PhI) program.

The ultimate goal of BIGTOP is to realize a Sagnac interferometer with an enclosed area of 100 mm^2 using multiple orbits in an $\omega_\rho = 2\pi \times 2$ Hz TOP trap. While a compact and semi-portable system is being developed offsite, we are working towards implementing improvements and making a BEC and Sagnac interferometer with a new system, an upgraded version of the present apparatus. We refer to this version as V1. Much of the current setup will remain unchanged from the work described so far. The biggest change will be replacing the cube trap geometry we use in this work with a "chip" trap, where strong magnetic fields are produced with a micro-fabricated

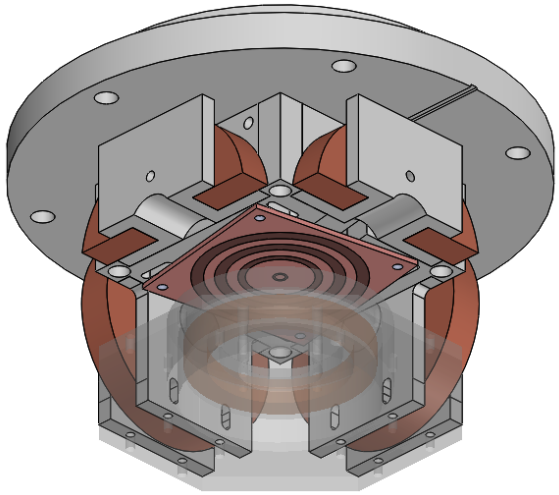

Figure 5.1: **A 3D CAD rendering of the V1 chip holder.** A bias coil is cutaway here along $\hat{\mathbf{x}}$ and $\hat{\mathbf{y}}$ to better show the assembly. A z coil is mounted below the chip, shown here transparently. The other z coil is mounted above the chip (not shown). The assembly is suspended underneath a water-cooled flange to improve temperature stability. Bragg beams and horizontal imaging axes lie within the horizontal bias coils.

coils that is mounted above the atoms. The chip is complemented by six cm-scale coils oriented orthogonally around the chip, which produce the same kind of bias fields used for the present work. The new version should allow for a tighter trap, which should allow for faster evaporative cooling and better thermal stability.

While progress towards achieving an improved interferometric rotation measurement in V1 continue at UVA, BIGTOP collaborators work on A-PhI Phase 2 goals. ColdQuanta, Inc. (CQ) is constructing a smaller semi-portable vacuum system to meet the size limitations imposed by the program. Northrop Grumman Missile Systems (NGMS) is developing the trap drive electronics, and will validate the performance of CQ's miniature system. Space Dynamics Laboratory (SDL) is developing models of the Bragg interferometer, and will analyze experimental results, and generate algorithms for improved performance. Additionally, Air Force Research Lab is

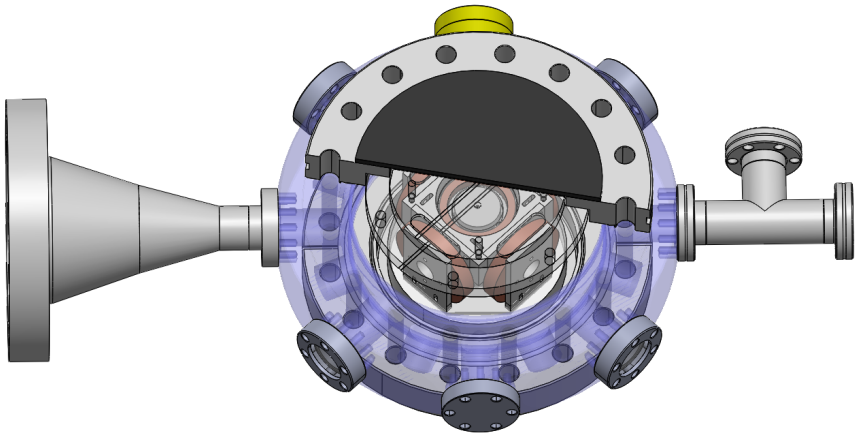

Figure 5.2: **A 3D CAD drawing of the planned science-side vacuum.** The top water-cooled flange is partially cutaway here to show the alumina chip and coil mounts. The octagonal vacuum chamber is displayed in blue to differentiate it from other components. Bragg beams cross the condensate diagonally through the 1.33 inch windows. All of the coils and chip signals enter through a feedthrough via the conical adapter, where the ion pump and TSP are also housed. The RF antenna comes in through the T on the right and is positioned with its axis of symmetry pointing towards the MOT (to the right here), fixed with a Kimball Physics Groove Grabber. The yellow component is a SAES NEG pump to improve vacuum. We expect V1 to eclipse the accuracy and stability of the cube trap. A few things are most important, and I will go through them now.

contributing with the fabrication of the chip.

For V1, the experiment will remain unchanged until the atoms are translated from the MOT side to the science side. To house the chip and the six additional coils, a mount was designed and machined from aluminum nitride. The chip and coils are mounted to a water-cooled flange. The flange is mounted to a circular vacuum chamber with eight symmetric optical access points. A window is fitted to the bottom of the vacuum, giving us imaging access of the xy plane using a silicon mirror glued to the chip. The V1 chip assembly is shown in Fig. 5.1. At the time of this writing, thermal tests on the constructed assembly shown in Fig. 5.2 are underway, after which the full vacuum will be assembled and put under ultra-high vacuum.

5.3 Thermal management and duty cycle

As discussed in the previous chapter, trap heating can cause headaches. Interferometry becomes challenging if the trap frequencies change as the experiment runs, especially when the parameter space has to be very well-optimized to see interference. Simple tasks like trap characterization also become difficult as the trap changes in time. With the lessons from the cube trap, care is being taken to ensure the chip trap will not suffer from similar problems.

The aluminum nitride (Shapal Hi-M Soft) support structure has good thermal conductivity, with enough surface area to keep the trap heating to under 10 K running at full power in a 60 second duty cycle. The support structure is mounted to a steel flange with air-side water cooling. The aluminum nitride coil mounts are glued together to help dissipate thermal energy. We will use new current sources for the

trap drive circuit, which were constructed by NGMS. With the thermal improvements and more stable electronics, we expect the long-term amplitude drifts to be less than 10^{-4}.

5.4 Optical access

One of the most significant problems with the old trap was optical access along the y direction. Because the Bragg beam passed through the full length of the chamber, it was difficult to align and retro-reflect. One of the big advantages to the x Bragg beam was that it shared its axis with the side camera imaging system. The complications from having these beam paths collinear were discussed in Chapter 2, but the advantages far outweighed these concerns. As described in Chapter 2, we are able to use the camera to align the Bragg beam onto the atoms. In the V1 apparatus, we will be able to easily align both Bragg beams using this technique, and the problems arising from the long y Bragg beam path will not be an issue. The bias coils are oriented such that the Bragg axes are diagonal to the track, and it will be convenient to set up imaging axes along both $\hat{\mathbf{x}}$ and $\hat{\mathbf{y}}$. We will be able to swap the side camera between the xz plane and the yz plane.

Figure 5.3 shows the new side imaging configuration. Both the Bragg and probe beams will be delivered to the experiment on the same optical fiber, so there will be no need for polarizing optics that can introduce power fluctuations and instability. The system is designed to be able to swap the side camera from $\hat{\mathbf{x}}$ to $\hat{\mathbf{y}}$, with removable probe optics downstream of the BEC so the Bragg retro mirror can remain in place. This system should help in a few ways. The first is alignment, which will be similar

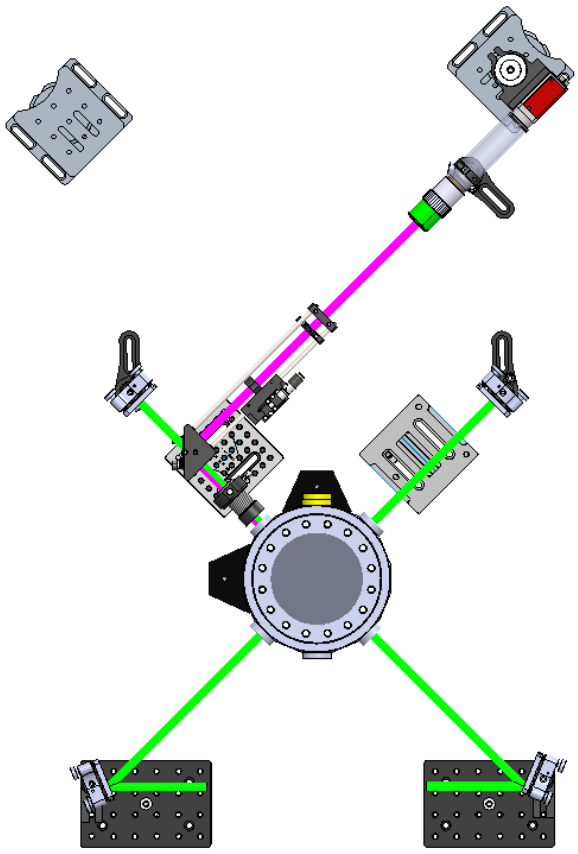

Figure 5.3: **An overhead view of the V1 side imaging and Bragg optics.** The Bragg beams are shown in green, and the probe beam is shown in pink. The side camera is mounted on a movable base (Newport BKL-4) to be swapped between the two side imaging planes. The optics redirecting the probe beam towards the camera are also on a magnetic base (Thorlabs KBM1) Here, the system is setup to image the xz plane with the x Bragg beam unblocked.

along the horizontal directions since we can image the condensate and the Bragg beams. The second is the shorter beam path. The retro-mirror will now both be around 20 cm behind the condensate, similar to the distance to the x retro-mirror in the cube trap.

With the chip oriented above the atoms, the Apogee camera will be repositioned to image from below the vacuum chamber. We expect this should also cut down further on vibrational noise in the imaging system. To make room for the camera optics and to give users much-needed room underneath the experiment, we will lift the experiment 4.5" off the table. That also gives more room underneath the translating dc coils. In the original system, the bottom MOT beam clipped on the magnetic coils, which we will now be able to avoid.

Good progress towards the complete V1 apparatus is being made. We expect to have a working interferometer in the next few months. With that setup, we expect the phase sensitivity to be 100 mrad $\cdot$ s$^{1/2}$. In the next twelve months we expect to have the compact CQ system in-hand, which should provide phase sensitivity of 30 mrad $\cdot$ s$^{1/2}$. In conclusion, the work described in this thesis was the first step towards a matter-wave rotation sensor with useful performance standards.

Appendices

A ⁘ Twitch routines

This chapter is included for readers interested in a detailed understanding of the rotation measurement. Twitch is the name of Casslab's homebuilt GUI, which compiles all experimental scripts. Compiled routines are then run by the Adwin II computer, which controls a number of experimental hardware, with the ability to simplify scripts with precompiled subroutines. Other experimental hardware, viz. the two cameras and the RF function generator, are controlled by a different program called Commander via rs232 commands in Twitch. Commander routines are all contained in a file named "evap.txt," which lives in the same directory as Commander. These are called by Twitch as "rs232 x," where x is a roman letter. Twitch also has the three inputs, which are used to interlock the beginning of the experiment to the MOT level, and to sync the experiment with the rising edge of the bias field to ensure the trap fields are consistent run-to-run.

The structure of each Twitch file has three components. From left to right, each line of the experiment has the duration of the step, the digital channels, then eight analog channels. For subroutines, rs232 commands, and digital inputs, the line simply lists the name of step. For analog channels, quotation marks (") are used when there is no change from the previous line. Quotation marks are also used in the digital

channels for the same purpose, but digital channels can be added or subtracted. If the duration of the experimental step includes `r`, that indicates there is an analog voltage that is ramped linearly from its previous value.

A.1 ADWIN

There are 24 digital channels with BNC outputs. Each channel has a three-position switch. When left in the center position, the output is controlled by the Twitch file. The other two positions are used to override Twitch to force the channel low or high. Note that all shutters listed are set such that high corresponds to the shutter being open to allow light through. There are eight analog outputs, labeled here as V_1 through V_8. They can supply a voltage $|V| \leq 10$. There are three digital inputs. Those are used to trigger the experiment with three different external timebases.

A.1.1 Digital inputs

a	Track	Low: MOT side, high: Science side
b	Bias field	
c	DC quadrupole IGBT	
d	MOT shutters	
e	General trigger	
f		(Broken)
g	Pump AOM	
h	Master shutter	
i	MOT AOM	Normally high
j	EOM digital 1	j = MOT, jk = CMOT, k = pumping
k	EOM digital 2	
l	Pump shutter	
m		
n	Linear actuator trigger	
o		
p	Probe shutter	
q		
r		
s	x Bragg shutter	
t	y Bragg shutter	
u		
v	Waveguide digital control	
w	Camera triggers	
x	rs232 TX	transmits rs232 data

A.1.2 Analog outputs

1	2× AOM frequency	19.5 MHz/V/pass; 0 V ↔ 45.9 MHz
2	Quadrupole current control	-0.02 V ↔ 0 A, 10 V ↔ 750 A
3	Bragg AOM	
4	Probe AOM	
5	x Bias amplitude modulation	-5 V ↔ off, 5 V ↔ on
6		
7	Waveguide bias amplitude	
8	Waveguide quadrupole amplitude	

A.1.3 Inputs

Event in	loadMOT interlock	resets to 90% of the current MOT level
DIO 24	rs232 rx	receives rs232 data
DIO 25	sync25	60 Hz sync
DIO 26	sync26	x bias field sync

A.2 Dual Sagnac interferometer

This is the full routine for dual Sagnac interference measurement. Variables are listed as they are in the text of this thesis in lieu of experimental values. In particular, the time between the splits, t_1, and the interferometer time t_2, are spread across two or three steps. That is done to ensure the shutters are closed for as long as possible to avoid leakage light. The last step, t_{wait}, is the time between runs, which is normally around 60 seconds to allow the waveguide to cool down. Note that the linear actuator causing the table to rotate is triggered in the `Loadguide` subroutine.

Time / Routine	Digitals	V_1	V_2	V_3	V_4	V_5	V_6	V_7	V_8
loadMOT									
Setup									
MOT									
Pumping									
Magtrap									
Movetrap_BEC									
Evaporate									
Loadguide									
5	"+t	"	"	0	"	"	"	"	"
Y_split									
$t_1 - 5$	"+t	"	"	0	"	"	"	"	"
5	"+s-e	"	"	"	"	"	"	"	"
X_split									
$t_2 - 15$	"-s	"	"	0	"	"	"	"	"
10	"+w	"	"	"	"	"	"	"	"
5	"+s	"	"	"	"	"	"	"	"
X_split									
7	"-s	"	"	0	"	"	"	"	"
Imaging									
MOT_reset									
t_{wait}	"	"	"	"	"	"	"	"	"

A.2.1 Pumping

Time / Routine	Digitals	V_1	V_2	V_3	V_4	V_5	V_6	V_7	V_8
1	cdhije	0	0.25	0	0	0	0	0	0
10r	"+k	1.2	"	"	"	"	"	"	"
0.001	"	"	"	"	"	"	"	"	"
8	"-c	"	0	"	"	"	"	"	"
2	"-d+l	"	"	"	"	"	"	"	"
0.5r	"+b-j	0.1	"	"	"	"	"	"	"
0.5	bghlk	"	"	"	"	"	"	"	"
0.001	"-g-l-k	"	"	"	"	"	"	"	"
1r	"	0	"	"	"	"	"	"	"

A.2.2 Magtrap

Time / Routine	Digitals	V_1	V_2	V_3	V_4	V_5	V_6	V_7	V_8
40	cb	0	2.5	0	0	5.0	0	0	0
0.01	"+i	"	"	"	"	"	"	"	"
200r	"	"	10	"	"	"	"	"	"

A.2.3 Movetrap_BEC

Time / Routine	Digitals	V_1	V_2	V_3	V_4	V_5	V_6	V_7	V_8
2000	cai	"	"	"	"	"	"	"	"

A.2.4 Evaporate

Time / Routine	Digitals	V_1	V_2	V_3	V_4	V_5	V_6	V_7	V_8
rs232 b									
rs232 0									
sync25									
sync26									
100	"+v	"	"	"	"	4.5	"	"	"
1000	"+i	"	"	"	"	"	"	10	"
300r	"	"	"	"	"	"	"	8	"
4993r	"	"	"	"	"	"	"	3.05	"
rs232 c									
rs232 0									

A.2.5 Loadguide

Time / Routine	Digitals	V_1	V_2	V_3	V_4	V_5	V_6	V_7	V_8
sync25									
sync26									
0.001	"	0	10	0	0	4.5	0	3.05	0
200r	"	"	8	"	"	2.0	"	"	7.5
200r	"	"	5	"	"	"	"	"	7.5
400r	"	"	1.5	"	"	"	"	"	7.5
1500r	"	"	1	"	"	"	"	"	8
2000r	"	"	0.7	"	"	"	"	1	8.25
2000r	"	"	0.1	"	"	"	"	"	8.5
3000r	"	"	0.01	"	"	"	"	"	8.75
3000r	"	"	-0.02	"	"	"	"	"	"
150	"+n	"	"	"	"	"	"	"	"
10	"-n	"	"	"	"	"	"	"	"

A.2.6 X_split

This is the subroutine that is used to split the condensate along $\hat{\mathbf{x}}$, following the three-step splitting procedure in [42]. The fidelity of the split is adjusted with V_{x1} and V_{x2} such that all the atoms in are moved into the momentum states. The x Bragg shutter is opened and closed in the main routine.

Time / Routine	Digitals	V_1	V_2	V_3	V_4	V_5	V_6	V_7	V_8
0.02168	"	"	"	V_{x1}	"	"	"	"	"
0.03644	"	"	"	V_{x2}	"	"	"	"	"
0.02168	"	"	"	V_{x1}	"	"	"	"	"

A.2.7 Y_split

This is largely the same as the previous subroutine. The AOM voltages V_{y1} and V_{y2} are different from those for the x-split, but are optimized for ideal splitting along $\hat{\mathbf{y}}$. Again, the shutter is opened and closed in the main routine.

Time / Routine	Digitals	V_1	V_2	V_3	V_4	V_5	V_6	V_7	V_8
0.02168	"	"	"	V_{y1}	"	"	"	"	"
0.03644	"	"	"	V_{y2}	"	"	"	"	"
0.02168	"	"	"	V_{y1}	"	"	"	"	"

A.2.8 Imaging

This is the imaging subroutine. After the waveguide is turned off, the cloud undergoes ballistic expansion on the fifth line, which is normally set to zero. On lines seven and ten, the atoms image and the no-atoms image are taken, respectively. The Probe AOM voltage V_{probe} sets the amount of light in each image.

Time / Routine	Digitals	V_1	V_2	V_3	V_4	V_5	V_6	V_7	V_8
0	"	0	-0.02	0	0	2	0	1	8.75
0.05r	"	0.5	"	"	"	2.0	"	"	0
0.05r	"	0.5	"	"	"	2.0	"	0	"
0.1	"-c-v	0.5	"	"	"	2.0	"	"	"
0	"	"	"	"	"	"	"	"	"
5	"+h-i+p	"	"	"	"	"	"	"	"
0.05	"	"	"	"	V_{probe}	"	"	"	"
100	"-h+i-p	"	"	"	0	"	"	"	"
5	"+h-i+p	"	"	"	"	"	"	"	"
0.05	"	"	"	"	V_{probe}	"	"	"	"
5	"-h-i-p+j	"	"	"	0	"	"	"	"
4000	"	"	"	"	"	"	"	"	"

A.2.9 MOT_reset

Time / Routine	Digitals	V_1	V_2	V_3	V_4	V_5	V_6	V_7	V_8
40	cb	0	2.5	0	0	5.0	0	0	0

Bibliography

[1] M. H. Anderson, J. R. Ensher, M. R. Matthews, C. E. Wieman, and E. A. Cornell. Observation of Bose-Einstein Condensation in a Dilute Atomic Vapor. *Science*, 269(5221):198–201, 1995.

[2] K B Davis, M O Mewes, M R Andrews, N J van Druten, D S Durfee, D M Kurn, and W Ketterle. Bose-Einstein condensation in a gas of sodium atoms. *Phys. Rev. Lett.*, 75:3969, 1995.

[3] C. C. Bradley, C. A. Sackett, J. J. Tollett, and R. G. Hulet. Evidence of Bose-Einstein Condensation in an Atomic Gas with Attractive Interactions. *Phys. Rev. Lett.*, 75(9):1687–1690, 1995.

[4] R. Onofrio, C. Raman, J. M. Vogels, J. R. Abo-Shaeer, A. P. Chikkatur, and W. Ketterle. Observation of Superfluid Flow in a Bose-Einstein Condensed Gas. *Phys. Rev. Lett.*, 85(11):2228, 2000.

[5] M. Greiner, O. Mandel, T. Esslinger, T. W. Hänsch, and I. Bloch. Quantum Phase Transition From a Superfluid to a Mott Insulator in a Gas of Ultracold Atoms. *Nature*, 415(6867):39–44, 2002.

[6] G. Roati, E. De Mirandes, F. Ferlaino, H. Ott, G. Modugno, and M. Inguscio. Atom Interferometry With Trapped Fermi Gases. *Phys. Rev. Lett.*, 92(23):230402, 2004.

[7] M. Moldwin. *An Introduction to Space Weather*, volume 1. Cambridge University Press Cambridge, 2008.

[8] T. L. Gustavson, A. Landragin, and M. A. Kasevich. Rotation Sensing With a Dual Atom-Interferometer Sagnac Gyroscope. *Class. Quantum Grav.*, 17:2385, 2000.

[9] D. S. Durfee, Y. K. Shaham, and M. A. Kasevich. Long-Term Stability of an Area-Reversible Atom-Interferometer Sagnac Gyroscope. *Phys. Rev. Lett.*, 97:240801, 2006.

[10] D. Savoie, M. Altorio, B. Fang, L. A. Sidorenkov, R. Geiger, and A. Landragin. Interleaved Atom Interferometry for High-Sensitivity Inertial Measurements. *Sci. Adv.*, 4, 2018.

[11] G. Lamporesi, A. Bertoldi, L. Cacciapuoti, M. Prevedelli, and G. M. Tino. Determination of the Newtonian Gravitational Constant Using Atom Interferometry. *Phys. Rev. Lett.*, 100:050801, 2008.

[12] A. Wicht, E. Hensley, J. M. Sarajlic, and S. Chu. A Preliminary Measurement of the Fine Structure Constant Based on Atom Interferometry. *Physica Scripta*, T102:82, 2002.

[13] S. Dimopoulos, P. W. Graham, J. M. Hogan, M. A. Kasevich, and S. Rajendran. Gravitational Wave Detection With Atom Interferometry. *Phys. Rev. B*, 678(1):37–40, 2009.

[14] G. Sagnac. L'éther Lumineux Démontré par L'éffet du Went Relatif D'éther Dans un InterféRometre en Allan Variance Analysis Rotation Uniforme. *C. R. Acad. Sci.*, 95:708, 1913.

[15] L. Zhou, Z. Y. Xiong, W. Yang, B. Tang, W. C. Peng, K. Hao, R. B. Li, M. Liu, J. Wang, and M. S. Zhan. Development of an Atom Gravimeter and Status of the 10-Meter Atom Interferometer for Precision Gravity Measurement. *General Relativity and Gravitation*, 43(7):1931–1942, 2011.

[16] T. Kovachy, P. Asenbaum, C. Overstreet, C. A. Donnelly, S. M. Dickerson, A. Sugarbaker, J. M. Hogan, and M. A. Kasevich. Quantum Superposition at the Half-Metre Scale. *Nature*, 528(7583):530–533, 2015.

[17] W. Ketterle and D. E. Pritchard. Trapping and Focusing Ground-State Atoms With Static Fields. *Appl. Phys. B*, 54:403, 1992.

[18] J. A. Sauer, M. D. Barrett, and M. S. Chapman. Storage ring for neutral atoms. *Phys. Rev. Lett.*, 87:270401, Dec 2001.

[19] A. S. Arnold. Adaptable-Radius, Time-Orbiting Magnetic Ring Trap for Bose-Einstein Condensates. *J. Phys. B: At. Mol. Opt. Phys.*, 37:L29, 2004.

[20] M. Horikoshi and K. Nakagawa. Suppression of Dephasing due to a Trapping Potential and Atom-Atom Interactions in a Trapped-Condensate Interferometer. *Phys. Rev. Lett.*, 99:180401, Oct 2007.

[21] S. R. Segal, Q. Diot, E. A. Cornell, A. A. Zozulya, and D. Z. Anderson. Revealing Buried Information: Statistical Processing Techniques for Ultracold-Gas Image Analysis. *Phys. Rev. A*, 81:053601, 2010.

[22] V. Vali and R. W. Shorthill. Fiber Laser Gyroscopes. In *Fibers and Integrated Optics*, volume 0077.

[23] G. B. Jo, Y. Shin, S. Will, T. A. Pasquini, M. Saba, W. Ketterle, D. E. Pritchard, M. Vengalattore, and M. Prentiss. Long Phase Coherence Time and Number Squeezing of Two Bose-Einstein Condensates on an Atom Chip. *Phys. Rev. Lett.*, 98:030407, 2007.

[24] S. Wu, E. Su, and M. Prentiss. Demonstration of an Area-Enclosing Guided-Ataom Interferomter for Rotation Sensing. *Phys. Rev. Lett.*, 99:173201, 2007.

[25] J.H. T. Burke and C. A. Sackett. A Scalable Bose-Einstein Condensate Sagnac Interferometer in a Linear Trap. *Phys. Rev. A*, 80:061603(R), 2009.

[26] L. Qi, H. Zhaohui, T. Valenzuela, Y. Zhang, Y. Zhai, W. Quan, N. Waltham, and J. Fang. Magnetically Guided Cesium Interferometer for Inertial Sensing. *App. Phys. Lett.*, 110:153502, 2017.

[27] M. Boshier, private communication (2019).

[28] E. Moan, Z. Luo, and C. A. Sackett. A Large-Area Sagnac Interferometer Using Atoms in a Time-Orbiting Potential. In *Proc. SPIE 10934, Optical, Opto-Atomic, and Entanglement-Enhanced Precision Metrology, 109341X*, page 10.1117/12.2515457, New York, 2019. IEEE.

[29] R. A. Horne. *A Cylindrically Symmetric, Magnetic Trap for Bose-Einstein Condensate Atom Interferometry Applications.* PhD thesis, University of Virginia, 2015.

[30] T. Arpornthip. *Characterizing the Potential Energy of an Atom Trap Through Tomographic Fluorescence Imaging.* PhD thesis, University of Virginia, 2016.

[31] A. Fallon. *High Precision Measurements of the ^{87}Rb D Line Vector Polarizability.* PhD thesis, University of Virginia, 2020.

[32] Thorlabs, inc.

[33] Solidworks Student Package. Solidworks Corporation, 2019.

[34] This optical system was adapted from a version built by Nathan Lundblad at Bates College.

[35] M. A. de Araújo, R. Silva, E. de Lima, D. P. Pereira, and P. C. de Oliveira. Measurement of Gaussian Laser Beam Radius Using the Knife-Edge Technique: Improvement on Data Analysis. *Appl. Opt.*, 48(2):393–396, 2009.

[36] J. Dalibard and C. Tannoudji. Laser Cooling Below the Doppler Limit by Polarization Gradients: Simple Theoretical Models. *J. Opt. Soc. Am. B*, 6(11):2023–2045, 1989.

[37] E. Majorana. Atomi Orientati in Campo Magnetico Variabile. *Il Nuovo Cimento*, 9:43, 1932.

[38] W. Petrich, M. H. Anderson, J. R. Ensher, and E. A. Cornell. Stable, Tightly Confining Magnetic Trap for Evaporative Cooling of Neutral Atoms. *Phys. Rev. Lett.*, 74:3352, 1995.

[39] R. Leonard. *High Precision Measurement of the D-Line Tune-Out Wavelength in ^{87}Rb Using a Bose-Einstein Condensate Interferometer*. PhD thesis, University of Virginia, 2016.

[40] C. A. Schneider, W. S. Rasband, and K. W. Eliceiri. NIH Image to ImageJ: 25 years of image analysis. *Nature Methods*, 9(7):671–675, 2012.

[41] SJ Wu, YJ Wang, Q Diot, and M Prentiss. Splitting matter waves using an optimized standing-wave light-pulse sequence. *Phys. Rev. A*, 71:043602, 2005.

[42] K. J. Hughes, B. Deissler, J. H. T. Burke, and C. A. Sackett. High-Fidelity Manipulation of a Bose-Einstein Condensate Using an Optical Standing Wave. *Phys. Rev. A*, 76:035601, 2007.

[43] R. A. Horne and C. A. Sackett. A Cylindrically Symmetric Magnetic Trap for Compact Bose-Einstein Condensate Atom Interferometer Gyroscopes. *Rev. Sci. Instrum.*, 88:013102, 2017.

[44] J. D. Jackson. *Classical Electrodynamics*. Wiley, New York, 3rd edition, 1999.

[45] K. L. Baranowski and C. A. Sackett. A Stable Current Source for Magnetic Traps. *J. Phys. B: At. Mol. Opt. Phys.*, 39:2949–2957, 2006.

[46] L. D. Landau and E. M. Lifshitz. *Mechanics*. Pergamon, New York, 3rd edition, 1960.

[47] L. D. Landau and E. M. Lifshitz. *Statistical Physics*. Pergamon, London, 1st edition, 1958.

[48] F. Dalfovo, S. Giorgini, L. Pitaevskii, and S. Stringari. Theory of Bose-Einstein Condensation in Trapped Gases. *Rev. Mod. Phys.*, 71:463, 1999.

[49] A. D. West. Systematic Effects in Two-Dimensional Trapped Matter-Wave Interferometers. *Phys. Rev. A*, 100(6):063622, 2019.

[50] Y. J. Wang, D. Z. Anderson, V. M. Bright, E. A. Cornell, Q. Diot, T. Kishimoto, M. Prentiss, R. A. Saravanan, S. R. Segal, and S. Wu. Atom Michelson Interferometer on a Chip Using a Bose-Einstein Condensate. *Phys. Rev. Lett.*, 94:090405, 2005.

[51] O. Garcia, B. Deissler, K. J. Hughes, J. M. Reeves, and C. A. Sackett. Bose-Einstein-Condensate Interferometer With Macroscopic Arm Separation. *Phys. Rev. A*, 74:031601(R), 2006.

[52] Z. Lou. *Simulations and Designs for Atom Interferometry Experiments*. PhD thesis, University of Virginia, 2020.

[53] E. R. Moan, R. A. Horne, T. Arpornthip, Z. Luo, A. J. Fallon, S. J. Berl, and C. A. Sackett. Quantum Rotation Sensing with Dual Sagnac Interferometers in an Atom-Optical Waveguide. *Phys. Rev. Lett.*, 124:120403, 2020.

[54] M. S. Grewal, A. P. Andrews, and C. G. Bartone. *Global Navigation Satellite Systems, Inertial Navigation, and Integration*. Wiley, Hoboken, NJ, 3rd edition, 2013.

[55] A. Fallon, R. H. Leonard, and C. A. Sackett. Estimation of Phase Diffusion Rates in a Condensate Interferometer Using the Gross-Pitaevskii Equation. *J. Phys. B*, 48:205301, 2015.